


Cross section measurements of proton capture reactions on Se isotopes relevant to the astrophysical p process

V. Foteinou,^{*} S. Harissopulos,[†] M. Axiotis, A. Lagoyannis, G. Provatias, A. Spyrou,[‡] G. Perdikakis,[§] and Ch. Zarkadas^{||}
Tandem Accelerator Laboratory, Institute of Nuclear and Particle Physics, NCSR “Demokritos”, 153.10 Aghia Paraskevi, Athens, Greece

P. Demetriou

Nuclear Data Section, International Atomic Energy Agency, Vienna 1400, Austria

 (Received 30 March 2016; revised manuscript received 3 December 2017; published 28 March 2018)

Cross sections of proton capture reactions on ^{74}Se , ^{78}Se , and ^{80}Se have been measured at incident beam energies from 2 to 6 MeV, 1.7 to 3 MeV, and 1.5 to 3.5 MeV, respectively. In the case of $^{78,80}\text{Se}$, cross sections were obtained from in-beam γ -angular distribution measurements, whereas for the ^{74}Se isotope they were derived from off-beam activity measurements. The measured cross sections were compared with calculations performed with the nuclear reaction code TALYS (version 1.6). A good agreement between theory and experiment was found. Astrophysical S factors and reaction rates deduced from the experimental and calculated cross sections were also compared and the impact of different nuclear ingredients in the calculations on the reaction rates was investigated. It was found that, for certain combinations of nuclear input models, the reaction rates obtained at temperatures relevant to p -process nucleosynthesis differ by a factor 2 at the most, differences that are well within the acceptable deviations of calculated p -nuclei abundances and observations.

DOI: [10.1103/PhysRevC.97.035806](https://doi.org/10.1103/PhysRevC.97.035806)

I. INTRODUCTION

The vast majority of the trans-iron nuclei are synthesized in the cosmos by the s and r processes [1,2] by either “slow” or “rapid” neutron radiative captures, respectively. In both cases, the (n,γ) reactions are followed by β^- decays of unstable nuclei produced either close or far away from the valley of stability. The “pathways” formed by these nuclear processes never cross 35 proton-rich stable nuclei lying between ^{74}Se and ^{196}Hg . These isotopes are known as p nuclei and their synthesizing mechanism is referred to in astrophysics as the p process [3].

As already comprehensively reviewed by Arnould and Goriely in [3], the p process evolves through a huge network of more than 20 000 nuclear reactions involving almost 2000 isotopes between iron and bismuth. This network comprises a huge number of coupled differential equations containing—as coefficients or unknown parameters—the decay rates of the involved unstable isotopes, the rates of the reactions through which nuclei are produced or destroyed and the abundances of the isotopes involved. The reactions entering the network are

neutron, proton, α -particle photodisintegrations, their competing capture reactions, as well as electron captures and β decays. Solving the network is required for the reproduction of the p -nuclei abundances in the stellar environment of interest.

The p -process network is taken [3] to operate at stellar temperatures between ≈ 1.8 and 3.3 billion degrees, i.e., at explosive stellar environments such as supernovae of type II (SN II) just before or during their explosion. Apart from that of a SN II site, some other stellar environments have been proposed as additional candidates hosting p -process nucleosynthesis. In some of these cases, additional types of nuclear reactions have been considered. Nevertheless, as of today, most of the latter scenarios are still under investigation and it is fair to say that any attempt to understand the origin of the p nuclei and the details of their creation in the cosmos still faces a major problem, i.e., to explain the discrepancies between the abundances of the p nuclei predicted by the various p process models and those observed in the solar system.

It is well accepted that successful calculations of p -nuclei abundances may deviate from the observed ones within an overall factor of 3 (see, e.g., in [3]). So far, however, none of the p -process models is capable of achieving this for all p nuclei; Instead there are some striking cases like, e.g., ^{92}Mo , for which the elimination of the strong discrepancies observed, partly up to two orders of magnitude, may require unrealistic parameters in the description of the astrophysical conditions. Such discrepancies indicate serious deficiencies either in the pure astrophysical modeling of the p process or they refer to large nuclear physics uncertainties entering the abundance calculations.

These considerations have motivated a large number of cross section measurements of proton capture reactions (see,

^{*}Present address: DTL/RUBION, Ruhr-Universität Bochum, Universitätsstrasse 150, 40781 Bochum, Germany.

[†]Corresponding author: sharisop@inp.demokritos.gr

[‡]Present address: NCSL, Michigan State University, East Lansing, MI 48824, USA.

[§]Present address: Department of Physics, Central Michigan University, Mount Pleasant, MI 48859, USA.

^{||}Present address: PANalytical B. V. Lelyweg 1, 7600AA Almelo, The Netherlands.

e.g., Refs. [4–6]), and to a lesser extent α -particle induced nuclear reactions at energies close or within the Gamow window associated to the p process. In the (p, γ) cases this window ranges from ≈ 1 to 5 MeV and is shifted to the ≈ 5 –12-MeV region for (α, γ) reactions. The primary goal of all these experimental studies is to investigate the nuclear physics uncertainties, i.e., to constrain all nuclear parameters, notably the optical model potentials (OMPs) and the nuclear level densities (NLDs) that are used to calculate theoretical cross sections within the statistical model for all reactions involved in the reaction network: Apparently, it is impossible to measure the cross sections of all these reactions, especially because their vast majority refers to unstable target nuclei. Instead, the Hauser-Feshbach (HF) theory [7] is almost exclusively used for this task.

The present paper reports on a systematic study of proton-induced reactions on Se isotopes. It complements our previous studies of capture reactions in nuclei with mass numbers A ranging from ≈ 60 to ≈ 120 .

II. EXPERIMENTAL SETUPS AND MEASUREMENTS

Three different sets of cross section measurements have been performed in the present work. In the first and second sets, the cross sections of the $^{78}\text{Se}(p, \gamma)^{79}\text{Br}$ and $^{80}\text{Se}(p, \gamma)^{81}\text{Br}$ reactions were determined for the first time from γ -ray angular distribution measurements. The energy of the proton beams, delivered by the 4-MV single-ended Dynamitron accelerator that operated previously at the University of Stuttgart, ranged from 1.5 to 3.5 MeV. In the third set of measurements, which have been carried out at the 5.5-MV T11/25 Van de Graaff Tandem Accelerator Laboratory of NCSR “Demokritos,” the activation technique was used to determine cross sections at energies from 2 to 6 MeV. The energy calibration of both accelerators was performed by nuclear magnetic resonance measurements (NMR) at the “plateau” of the 992-keV resonance of the $^{27}\text{Al}(p, \gamma)^{28}\text{Si}$ reaction, as described, e.g., in [8]. In both cases, the uncertainties in the incident proton energy did not exceed 2 keV.

A. γ -ray angular distribution measurements

The experimental setup consisted of four hyper-pure Ge (HPGe) detectors mounted on a rotating table at distances ranging from 13 to 20 cm from the target. The relative efficiency was almost 100% for the three of them and 76% for the fourth one. The Compton background was suppressed by using four BGO ($\text{Bi}_4\text{Ge}_3\text{O}_{12}$) crystals surrounding the Ge detectors. A detailed description of the experimental setup is given in [9].

By rotating the table by 15° in the case of $^{78}\text{Se}(p, \gamma)^{79}\text{Br}$, and 10° in the case of $^{80}\text{Se}(p, \gamma)^{81}\text{Br}$, γ -singles spectra were measured at eight angles with respect to the beam direction. At each angle, two different γ -singles spectra per detector were taken by guiding the corresponding pre-amplifier output signal into two different amplifiers of different gains that further fed two different analog-to-digital (ADC) converters. This way, a low- and a high-gain γ spectrum were obtained from each detector at each angle and beam energy. The former

spectrum included γ rays with energies up to ≈ 12.3 MeV in the case of $^{78}\text{Se}(p, \gamma)^{79}\text{Br}$ and ≈ 15.5 MeV for $^{80}\text{Se}(p, \gamma)^{81}\text{Br}$. These spectra were used to obtain mainly the yields of the corresponding primary γ transitions, i.e., γ rays deexciting the “entry state” of the produced nucleus. The high-gain spectrum included γ rays up to ≈ 4 MeV and was used for the analysis of secondary γ transitions, i.e., γ rays deexciting discrete levels that are fed by primary γ transitions and, as such, lie below the entry state. At each energy, additional spectra were taken at each one of the eight angles with the proton beam impinging on a blank backing, in order to investigate possible yield contributions from reactions occurring in the backing material. The latter were found to be negligible.

The absolute efficiency of our detector setup was determined as described in our previous papers (see in Refs. [9,10]). Furthermore, effects due to coincident summing were checked with a ^{57}Co radioactive source following the procedure described in [11] and found to be negligible. The targets used for the γ angular distribution measurements were prepared by evaporating highly enriched isotopic material onto 0.2-mm-thick tantalum disks with a 4-cm diameter. The isotopic enrichment of the ^{78}Se target was 97.8%, whereas that of ^{80}Se was 98%. The areal densities ξ of the targets, often referred to in the following as the “target thicknesses,” were determined using the x-ray fluorescence (XRF) technique (see, e.g., in [12,13]). The areal densities of the two ^{80}Se targets, which were placed at 90° with respect to the beam direction, were 106 ± 11 and $132 \pm 13 \mu\text{g}/\text{cm}^2$. The ^{78}Se target was placed at 105° to the beam axis; thus its effective areal density was $90 \pm 9 \mu\text{g}/\text{cm}^2$. According to the well-established code SRIM [14], the energy loss of a 3-MeV proton bombarding energy in these targets was 6, 7, and 5 keV, respectively.

During the measurements, the beam current ranged between 3 and 15 μA and the diameter of the almost circular beam spot was ≈ 4 mm. To avoid loss of target material due to target heating, the Ta backings were cooled directly with water throughout the measurements. Moreover, the thickness of the targets was checked at regular time intervals by collecting in-beam γ spectra at 2.4 and 2.5 MeV to compare the yields of some strong γ transitions from reactions induced on the target material by the proton beam: It was found that, within statistical errors ($\leq 5\%$), no target deterioration occurred.

Typical low gain γ -singles spectra of the $^{78}\text{Se}(p, \gamma)^{79}\text{Br}$ reaction measured at $E_p = 3$ MeV and the $^{80}\text{Se}(p, \gamma)^{81}\text{Br}$ reaction taken at $E_p = 1.7$ MeV are shown in Figs. 1 and 2, respectively. Both spectra were measured with the detector placed at an angle $\theta = 90^\circ$ with respect to the beam axis. Hereby, the peaks coming from γ transitions feeding the relevant ground state are all contained in panels (a) and are marked with numbers corresponding to their energy in keV. Both spectra include also peaks resulting from the $(p, p'\gamma)$ reaction of the proton beam on Ta (backings) and ^{23}Na . These peaks are labeled with the symbols ^{181}Ta and ^{23}Na , respectively. Moreover, the γ lines from the $(p, p'\gamma)$ reaction on the target isotopes are marked with ^{78}Se and ^{80}Se in Figs. 1 and 2, respectively. In both figures, there exist also peaks arising from the $^{19}\text{F}(p, \gamma)^{20}\text{Ne}$ and $^{19}\text{F}(p, \alpha\gamma)^{16}\text{O}$ reactions. ^{19}F is a common impurity in Ta foils, while ^{23}Na is usually deposited on the targets during their preparation. In addition, a

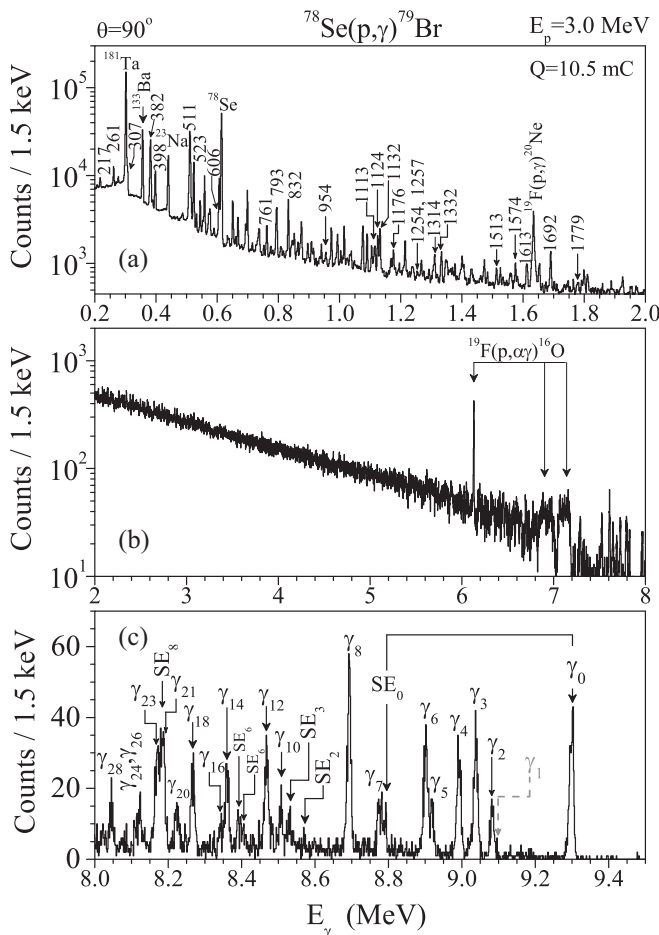


FIG. 1. Typical low gain γ spectrum of the $^{78}\text{Se}(p,\gamma)^{79}\text{Br}$ reaction measured at $E_p = 3$ MeV. The accumulated charge was 10.5 mC (see Sec. II A for details).

strong γ line at ≈ 3.5 MeV appears in panel (b) of Fig. 2. This peak arises from the $^{12}\text{C}(p,\gamma)^{13}\text{N}$ reaction resulting from the reaction of the protons impinging on the carbon deposited by the beam on the target surface.

The primary γ rays, i.e., the γ transitions depopulating the entry state of the produced ^{79}Br and ^{81}Br compound nuclei and feeding lower-lying discrete levels are indicated in panels (c) of Figs. 1 and 2 as γ_i . The integer index i indicates the accession number of the populated i th discrete state according to the level listing of [15] for ^{79}Br and ^{81}Br . Hence, the peak labeled as γ_0 in panels (c) of these figures is the primary γ transition to the corresponding ground states. It is worth emphasizing that γ_0 was present in all in-beam γ spectra collected in the present measurements. In Figs. 1 and 2, some single- (SE) or double-escape (DE) peaks are also visible. In the case of the primary γ transitions the corresponding peaks are labeled as SE_i and DE_i , respectively.

The peak in Fig. 1(a) labeled with ^{133}Ba is the 356-keV γ transition emitted by a ^{133}Ba radioactive source that was used as a “clock” to determine the corresponding dead time and accordingly correct the intensities of the peaks of interest. The vast majority of the unlabeled peaks shown in Figs. 1 and 2 refer to secondary γ transitions not feeding the ground state.

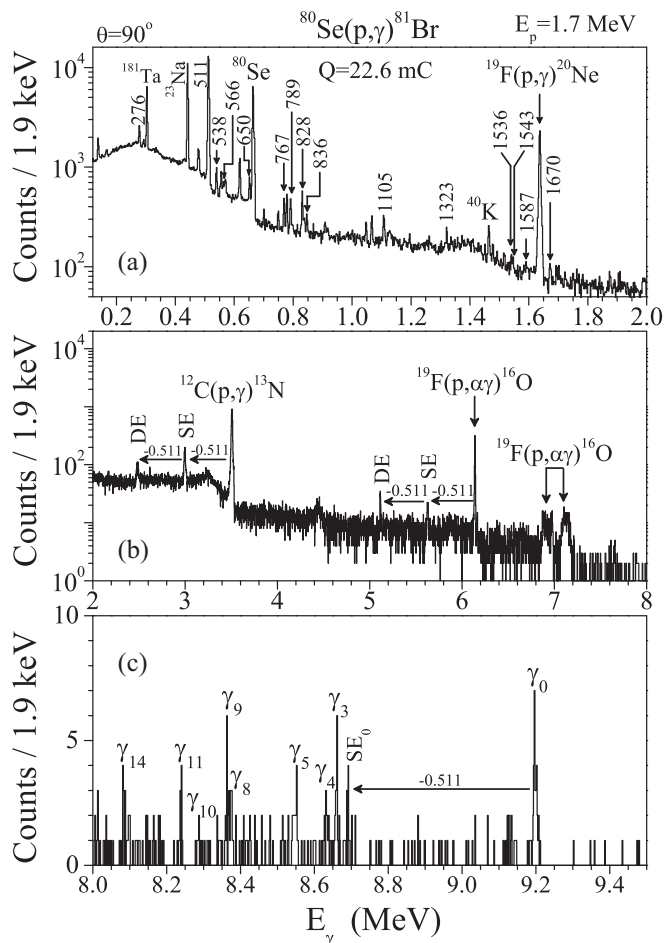


FIG. 2. Same as in Fig. 1 but for the $^{80}\text{Se}(p,\gamma)^{81}\text{Br}$ reaction measured at $E_p = 1.7$ MeV. The accumulated charge was $Q = 22.6$ mC (see Sec. II A for details).

It is worth noting that some primary γ transitions, such as the γ_1 and γ_9 in ^{79}Br expected to appear at energies 9.094 and 8.541 MeV, respectively, have not been observed in the spectra: The centroid of γ_1 is indicated in Fig. 1(c) by a dashed arrow and γ_9 should appear between the single-escape peaks SE_2 and SE_3 . The lack of some primary γ transitions in the spectra is to be attributed either to a very weak intensity or to the large spin difference between the entry and the corresponding final state that may suppress the connecting γ ray. The aforementioned γ_9 transition is a typical example of such a case: Because of the low energy of the beam, the projectiles are s -wave protons, i.e., their angular momentum l is zero. This value, in conjunction with the spin and parity of the ground state ($J^\pi = 0^+$) of the target nucleus ^{78}Se , results in a $J^\pi = 1/2^+$ entry state of the produced nucleus ^{79}Br . Since the ninth excited state of ^{79}Br has $J^\pi = 7/2^-$, the primary γ_9 transition would correspond to a spin difference $\Delta J \geq 3$, a difference that may explain the absence of this transition.

B. Activation measurements

Proton-induced compound nucleus (CN) reactions with a neutron-emission channel opening at relatively high energies

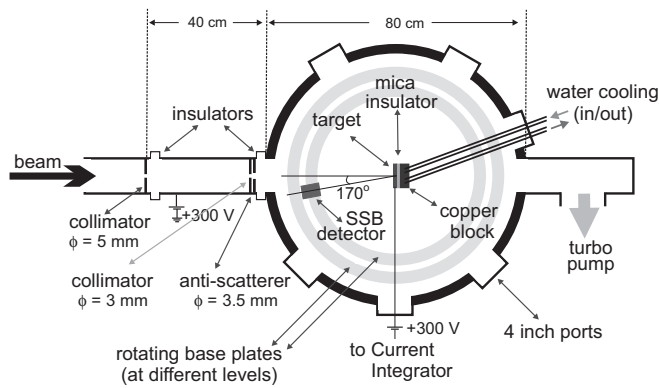


FIG. 3. Drawing of the scattering chamber employed in the activation measurements (see Sec. II B for details).

are best suited for a sensitive test of different optical model potentials (OMPs), since the (p,γ) channel is the strongest over a broad energy range. This is mostly the case when the target nucleus is the lightest isotope of the element of interest. Such a paradigm is the p nucleus ^{74}Se , for which the (p,n) channel has a threshold at 7.79 MeV. For comparison, the same threshold amounts to 5.82, 2.18, 4.41, 2.69, and 0.89 MeV for the heavier stable Se isotopes with mass number 76, 77, 78, 80, and 82, respectively.

Gyürky *et al.* [16] have already reported experimental (p,γ) cross sections on Se isotopes determined using the activation technique at proton energies E_p ranging from 1.3 to 3.6 MeV. The data published in this work for the case of ^{74}Se were in the 1.3–2.8-MeV range. Hence, the remaining “test” region up to 7.79 MeV has not been covered and this motivated the present activation measurements.

The experimental setup used in the present activation measurements is sketched in Fig. 3. It consists of a cylindrical scattering chamber made of aluminum with an outer diameter of 80 cm and a height of 35 cm. The chamber can host up to eight surface barrier detectors which are mounted onto aluminum rails so that their distance to the target can be adjusted by moving them on a rail. Samples to be irradiated were mounted on a target holder positioned at the center of the chamber that can move vertically. Every sample was cooled by a copper block attached on its back side. Between the sample and the block a thin mica foil was placed to achieve electrical, but not thermal, insulation. This way, targets are cooled indirectly by induction. The beam of the irradiating protons was collimated twice: the first collimator ($\varnothing = 5$ mm) downstream is located at a distance of ≈ 80 cm from the sample position, whereas the second one ($\varnothing = 3$ mm) is mounted at the entrance of the chamber followed by an anti-scatterer ($\varnothing = 3.5$ mm). They are all made of tantalum.

The samples used in our activation measurements had a diameter of ≈ 20 mm and were produced at the target preparation facility of the Tandem Accelerator Laboratory of NCSR “Demokritos” by evaporating metallic Se onto Al or Si wafers. The thickness of both backings was ≈ 0.3 mm. The areal densities of the Se layers were determined using the XRF technique [12,13] with an accuracy of $\approx 5\%$ and found to vary between 484 and 646 $\mu\text{g}/\text{cm}^2$. More details on the targets used

TABLE I. Areal densities ξ of the targets used in the irradiations of the present work at incident proton energies E_p . ΔE is the corresponding beam-energy loss in the target and Q is the charge accumulated by the end of the irradiations, whereas N_t is the number density of the ^{nat}Se target.

E_p (MeV)	Areal density ξ ($\mu\text{g}/\text{cm}^2$)	ΔE (keV)	Number density N_t (10^{16} at/ cm^2)	Q mC
2.0	604 ± 30	43	461 ± 23	12.8 ± 0.9
2.5	484 ± 24	30	369 ± 18	7.74 ± 0.54
3.0	539 ± 27	30	411 ± 21	8.45 ± 0.59
3.5	582 ± 29	30	444 ± 22	7.15 ± 0.50
4.0	555 ± 28	26	423 ± 21	6.55 ± 0.46
4.5	646 ± 32	28	493 ± 25	6.80 ± 0.48
5.0	534 ± 27	22	407 ± 20	2.12 ± 0.15
5.5	548 ± 27	21	418 ± 21	3.26 ± 0.23
6.0	486 ± 24	17	371 ± 19	1.89 ± 0.13

are given in Table I. During all irradiations, water cooling was applied to avoid material loss of the targets. Rutherford Backscattering Spectrometry (RBS) was, furthermore, applied to monitor the thickness and stability of the targets. For this purpose, RBS spectra were taken in frequent time intervals with a 300- μm -thick Si surface-barrier detector that was placed inside the chamber at a distance of ≈ 30 cm from the target and at an angle $\theta = 170^\circ$ with respect to the beam direction. From the comparison of the different RBS spectra it was found that target deterioration effects were not significant and were kept below 5%. A typical RBS spectrum is shown in Fig. 4.

The beam current ranged from 100 to 900 nA and was kept stable during each irradiation. The accumulated charge Q was measured with a current integrator (CI) and was subsequently digitized and recorded in multichannel scaling mode (MCS) within short time intervals Δt by using a “multiscaler”

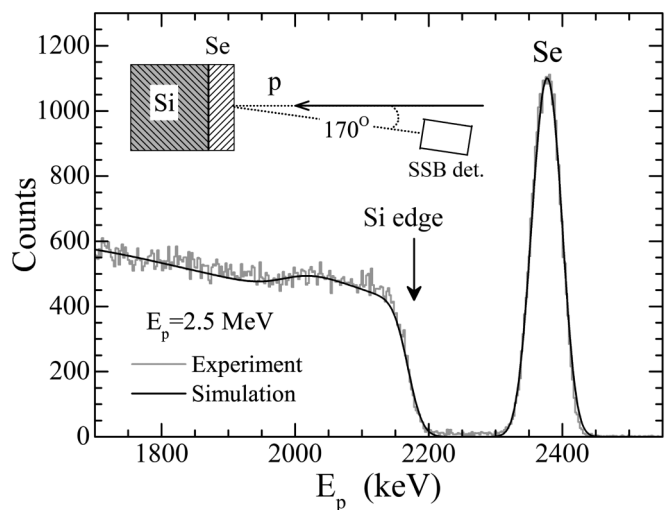


FIG. 4. Typical Rutherford backscattering spectrum (RBS) measured with a 2.5-MeV proton beam impinging on a 484- $\mu\text{g}/\text{cm}^2$ -thick ^{nat}Se layer evaporated on a 0.3-mm-thick Si wafer. The black solid curve is the corresponding simulation performed using the code SIMNRA [17].

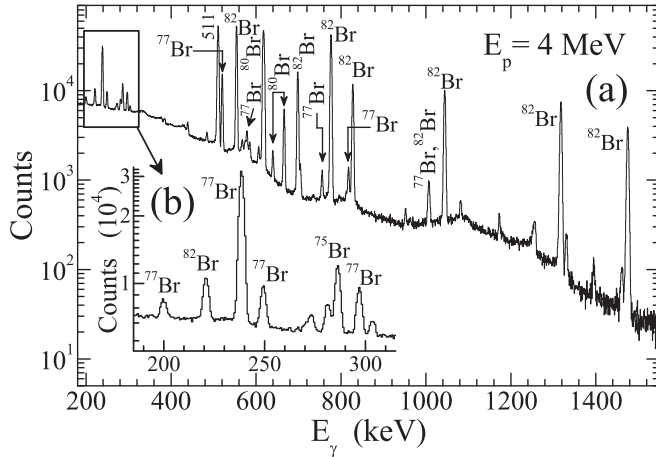


FIG. 5. Typical γ -activity spectrum taken at $E_p = 4$ MeV (see Sec. II B for details).

electronic unit connected directly after the CI to monitor the beam stability and correct for fluctuations of the beam flux Φ in the subsequent data analysis. The uncertainty of the CI reading was $\approx 7\%$, whereas the bins Δt were constantly 100 s. For a reliable current integration, a suppression voltage of +300 V was applied for the electrons emitted by the target and the beam collimator located at the entrance of the chamber, as shown in Fig. 3. The irradiation time (t_b) of the targets lasted 4 h in each beam energy.

The induced activity of the samples was measured after every irradiation with a HPGe detector, which was placed at a distance of ≈ 15 cm from the sample and was shielded with Pb blocks in order to reduce the background induced by natural radioactivity. Its relative efficiency was 50% and its absolute efficiency was determined using a calibrated ^{152}Eu source placed at the same sample position to ensure the same geometry conditions as in the activity measurements. The time interval t_w (“waiting time”) between the end of each irradiation cycle and the start of the off-beam activity measurements ranged from 6 to 15 min. A typical γ activity spectrum taken for ≈ 3.9 h after a 4-h-long irradiation of a $555\text{-}\mu\text{g}/\text{cm}^2$ -thick ^{nat}Se target with 4-MeV protons is shown in Fig. 5. Hereby, the strongest γ transitions are marked with the corresponding decaying “mother” isotope. Most of these peaks were used to extract cross sections.

III. DATA ANALYSIS AND RESULTS

A. γ -ray angular distribution measurements

The total cross section σ_T of a capture reaction measured by means of the γ -ray angular distribution technique is derived by

$$\sigma_T = \frac{A}{N_A \xi} Y, \quad (1)$$

where A is the atomic weight of the target in amu, N_A is the Avogadro number, ξ is the areal density of the target in g/cm^2 , and Y is the total reaction yield, i.e., the absolute number of the produced nuclei per beam particle. Y is the sum of the absolute

yields Y_i of all transitions feeding the ground state and is given by

$$Y = \sum_{i=1}^N Y_i = \sum_{i=1}^N A_0^i, \quad (2)$$

where N is the number of transitions feeding the ground state and A_0 are the absolute coefficients of the corresponding γ -angular distributions. The latter consist of data points $I(\theta, \epsilon, N_p)$ at a number of angles θ with respect to the beam axis, corrected for the absolute efficiency ϵ , the corresponding number of the incoming beam particles N_p , and dead time. N_p is determined from

$$N_p = Q/Zq_e, \quad (3)$$

where q_e is the charge of the electron, Z is the atomic number of the bombarding particles, here $Z = 1$, and Q is the accumulated charge determined by measuring the beam current and further integrating it over the measurement time by means of a current integrator. Hence,

$$I(\theta, \epsilon, N_p) = \frac{A(E_\gamma, \theta)}{\epsilon_\gamma(E_\gamma, \theta) t_d(\theta) Q}, \quad (4)$$

where t_d is the dead-time correction factor, A is the area under the peak of the γ transition with energy E_γ detected at angle θ , $\epsilon_\gamma(E_\gamma, \theta)$ is the corresponding detector efficiency, and Q is the accumulated charge.

The absolute A_0 coefficients, i.e., the absolute intensities of the γ transitions of interest, result from the fitting of the sum $W(\theta)$ of Legendre polynomials $P_n(\cos\theta)$ to the corresponding γ -angular distribution, i.e.,

$$W(\theta) = A_0[1 + a_2 P_2(\cos\theta) + a_4 P_4(\cos\theta)], \quad (5)$$

where the a_2 and a_4 coefficients result from the fit and depend on the angular momentum of the initial and final state.

Figures 6 and 7 depict the level schemes of ^{79}Br and ^{81}Br used in our data analysis to identify the γ transitions of interest. The numbers shown at the right of each level included in these figures indicate the corresponding excitation energy in keV, whereas the relevant spins and parities, if given in [15], are indicated at the left of the level.

In these figures, only the excited states feeding the ground state together with the corresponding transitions (dashed arrows) are included. These transitions are those that were taken into account to determine the cross sections by first determining Y from Eq. (2) and then applying Eq. (1). Depending on the energy of the incident protons, the energy of the entry states observed in the present work ranged between 8 and 9.3 MeV for the $^{78}\text{Se}(p, \gamma)^{79}\text{Br}$ reaction and from 8.99 to 10.98 MeV for $^{80}\text{Se}(p, \gamma)^{81}\text{Br}$.

In Fig. 7, an additional γ transition is shown with a curly arrow that deexcites the metastable state of ^{81}Br at 536.2 keV ($T_{1/2} = 34.6 \mu\text{s}$) and feeds its first excited state. This transition was included in the level scheme for completeness as it was analyzed in order to determine the corresponding partial cross section σ_m of the production of ^{81}Br in the aforementioned metastable state.

Typical γ -angular distributions measured in the present work for the ^{78}Se and ^{80}Se nuclei are shown in Figs. 8 and 9,

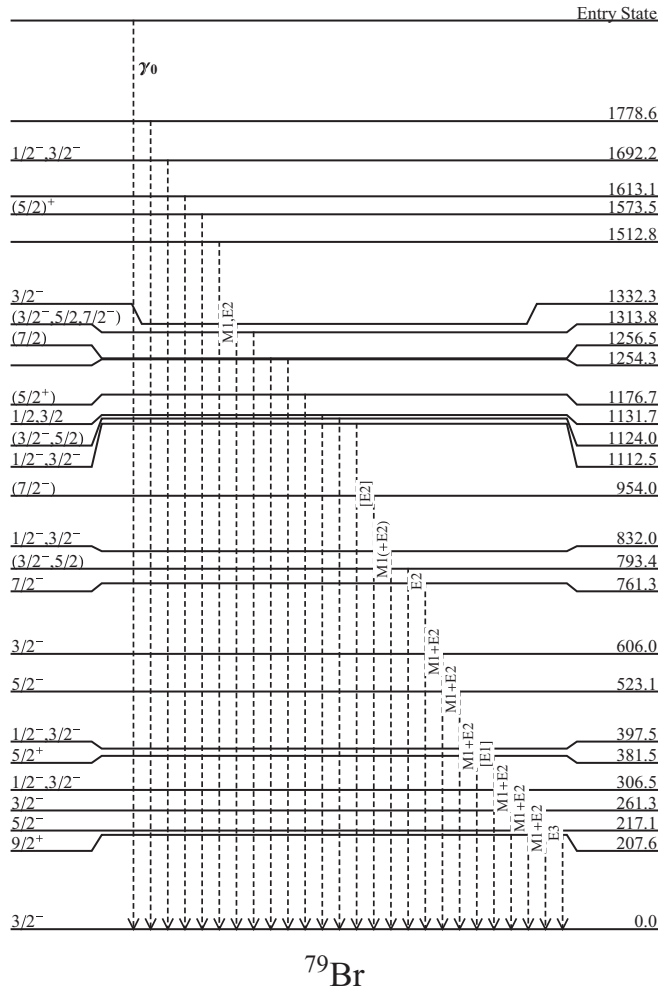


FIG. 6. Level scheme of the ^{79}Br nucleus containing all the γ transitions (dashed arrows) observed in the present work to populate its ground state. These transitions were used to determine the total cross section of the $^{78}\text{Se}(p, \gamma)^{79}\text{Br}$ reaction as described in Sec. III A.

respectively. As shown there, the angular distribution effects were almost negligible. In fact, fitting $W(\theta)$ [Eq. (5)] to almost 100 randomly selected γ -angular distributions, it was found that the resulting A_0 coefficients were within less than 5% equal to the weighted mean \bar{W} of the data points $I(\theta, \epsilon, N_p)$ of the corresponding γ -angular distribution. Hence, the absolute yields Y_i [Eq. (2)] of all (≈ 600) γ -angular distributions measured in the present work were derived by simply determining the corresponding \bar{W}_i values. In the case of the γ -angular distributions displayed in Figs. 8 and 9, the corresponding \bar{W} values are indicated with dashed horizontal lines.

The experimental total cross sections σ_T and the corresponding astrophysical S factors obtained from the γ -angular distribution measurements for the $^{78}\text{Se}(p, \gamma)^{79}\text{Br}$ and the $^{80}\text{Se}(p, \gamma)^{81}\text{Br}$ reactions are summarized in Table II. The errors given therein range between 10 and 15%. These are the result of error propagation in Eq. (1). Hereby, the relative uncertainties in the thicknesses ξ of the targets, the detector efficiency ϵ_γ , and the accumulated charge Q were 10%, $\approx 5\%$, and $\approx 3\%$, respectively, whereas that in the total yield Y ranged between

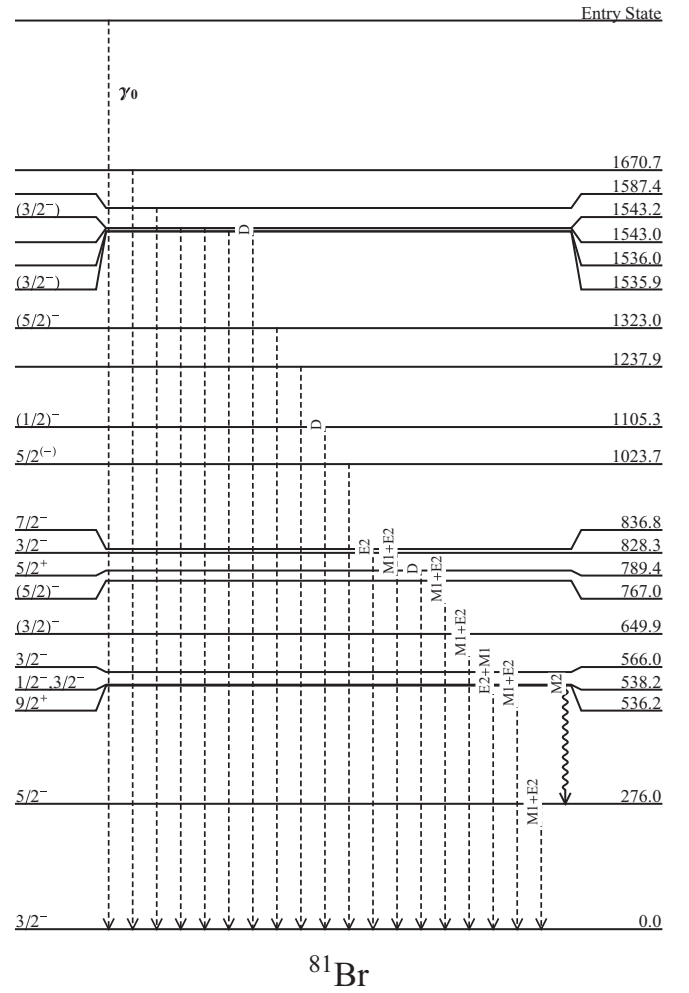


FIG. 7. Same as in Fig. 6 but for ^{81}Br .

3 and 30%. The latter refer to the relative errors in the weighted means in \bar{W}_i of the data points $I(\theta, \epsilon, N_p)$ of the different γ -angular distributions, which resulted from error propagation in Eq. (4).

Both the total cross sections σ_T and astrophysical S factors given in Table II are corrected for screening effects [18–20]. These effects result in an increase of the cross section and, hence, a correction is necessary. This was done by dividing the cross sections obtained from the γ -angular distributions with the electron screening factors f_s given [20] by

$$f(E) = \frac{E}{E + U_e} \exp\left(\frac{\pi \eta(E) Z_t Z_p U_e}{E}\right), \quad (6)$$

where U_e is the electron screening potential of ≈ 300 eV [18–20], E is the center-of-mass energy (in keV), Z_t and Z_p are the atomic number of the target and the projectile, respectively, and η is the Sommerfeld parameter [18] defined by

$$2\pi\eta = 31.29 Z_t Z_p \left(\frac{\mu}{E}\right)^{1/2}, \quad (7)$$

with the reduced mass μ in amu.

The electron screening factors f_s for the reactions investigated are also given Table II. The astrophysical S factors given

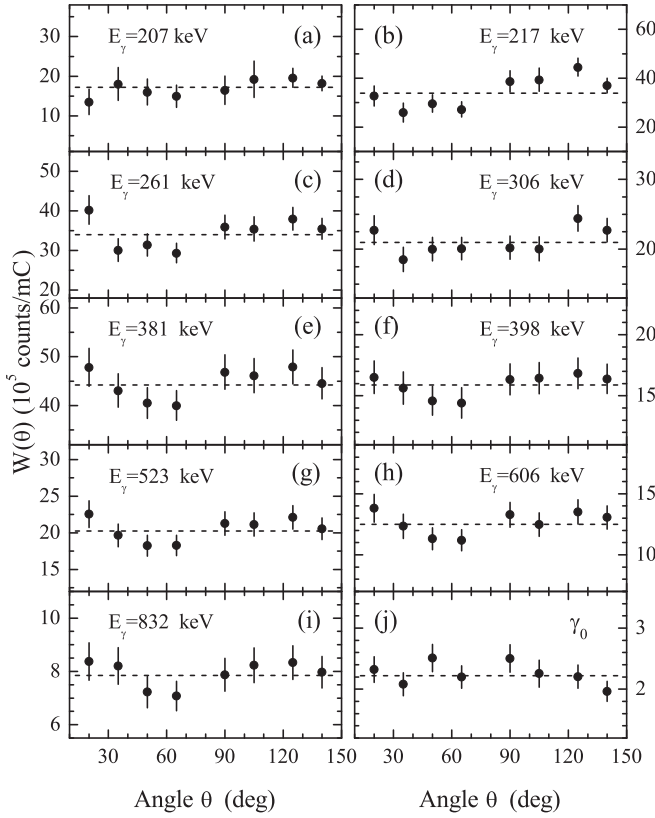


FIG. 8. Typical angular distributions of γ transitions of ^{79}Br measured at $E_p = 3$ MeV (see Sec. III A for details).

therein were determined from the electron-screening-corrected cross sections σ_T using

$$S(E) = \sigma_T(E) E e^{2\pi\eta(E)}. \quad (8)$$

The $E_{c.m.}$ values given in Table II are the corresponding effective beam energies E_{eff} in the center-of-mass system deduced from

$$E_{\text{eff}} = E_p - \frac{\Delta E}{2}, \quad (9)$$

where E_p is the incident proton beam energy and $\Delta E/2$ is its energy loss at the center of the target. The latter was derived from the stopping powers calculated with the code SRIM [14].

B. Activation measurements

Cross section measurements using the activation technique evolve in three discrete time intervals. In the first one, a target is irradiated for time t_b , depending on the half-life of the produced unstable “mother” nucleus that decays to the ground state or to one or more excited levels of a “daughter” nucleus, being usually a stable isotope. The excited states of the daughter are subsequently deexcited by emitting γ rays that populate lower-lying excited levels or the ground state. The detection of the latter γ transitions takes place during the third time interval, t_m (“measurement” or “counting” time). Usually, a short “waiting” time t_w intervenes between the irradiation of the samples and the measurement of the induced activity so

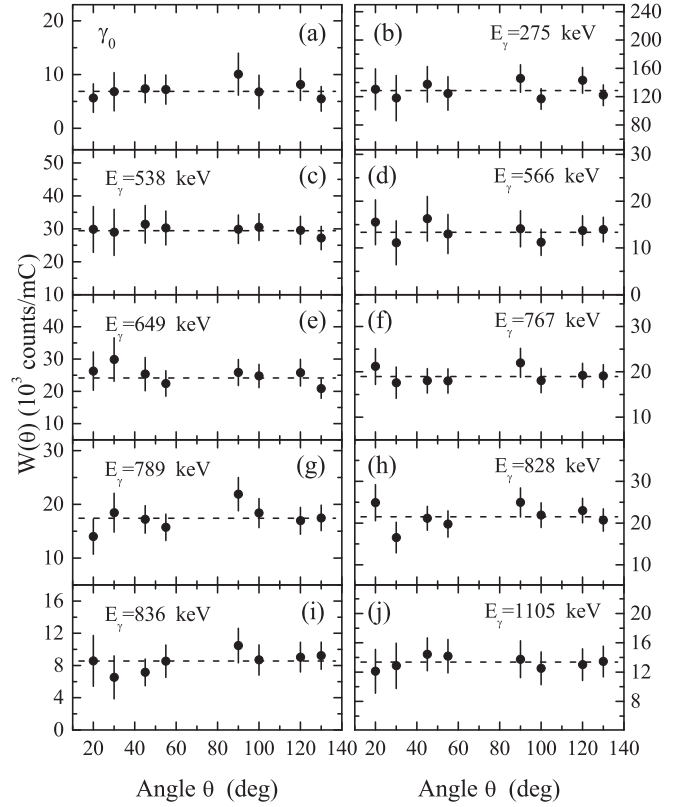


FIG. 9. Same as in Fig. 8 but for the ^{81}Br . The corresponding γ_0 transition is plotted in panel (a).

that the produced “hot” sample gradually “cools” and becomes easy to handle, or disturbing short-lived activities decay out.

The total cross section σ_T can be obtained from the intensity A_γ (net counts under the peak) of at least one of the γ transitions depopulating an excited state of the daughter nucleus. A_γ has to be corrected for dead time, absolute efficiency (ϵ_γ), cascade summing (k_s), self-absorption (k_γ) in case the thickness of the irradiated sample requires it, and possible pile-up effects. Using these quantities, the total number N_D of the daughter nucleus produced during the irradiation, which did not decay until the beginning of the counting cycle, is obtained by

$$N_D = \frac{A_\gamma}{t_d \epsilon_\gamma k_s k_\gamma I_\gamma}, \quad (10)$$

where I_γ is the relative γ -ray intensity per decay and t_d is the dead-time correction factor. N_D relates to the total number N_D^0 of the daughter nucleus produced during the irradiation time t_b with

$$N_D^0 = \frac{N_D e^{\lambda t_w}}{1 - e^{-\lambda t_m}}, \quad (11)$$

where λ is the decay constant of the produced unstable mother nuclei.

The cross section is derived from

$$\sigma = \frac{\lambda N_D^0}{N_i^0 (1 - e^{-\lambda \Delta t}) \left[\sum_{j=1}^n \Phi_j e^{-(n-j)\lambda \Delta t} \right]}, \quad (12)$$

TABLE II. Screening corrected total cross sections σ_T determined in the present work at various center-of-mass energies $E_{c.m.}$ together with corresponding astrophysical S factors and the screening correction factors f_s of the reactions $^{78}\text{Se}(p,\gamma)^{79}\text{Br}$ (first four columns) and $^{80}\text{Se}(p,\gamma)^{81}\text{Br}$ (last four columns). The uncertainties in $E_{c.m.}$ amount to 5 keV at the most.

$^{78}\text{Se}(p,\gamma)^{79}\text{Br}$				$^{80}\text{Se}(p,\gamma)^{81}\text{Br}$			
$E_{c.m.}$ (MeV)	σ_T (μb)	S factor (10^4 MeV b)	f_s	$E_{c.m.}$ (MeV)	σ_T (μb)	S factor (10^5 MeV b)	f_s
1.681	30.9 ± 3.6	904 ± 105	1.082	1.482	8.53 ± 1.03	119 ± 14	1.100
1.879	120 ± 13	968 ± 101	1.069	1.681	37.4 ± 4.0	110 ± 12	1.082
1.978	170 ± 18	775 ± 84	1.063	1.782	75.0 ± 8.2	111 ± 12	1.075
2.177	415 ± 43	682 ± 71	1.055	1.880	133 ± 15	107 ± 12	1.069
2.276	619 ± 65	644 ± 67	1.051	1.981	242 ± 26	109 ± 12	1.063
2.376	920 ± 96	625 ± 65	1.048	2.078	389 ± 43	104 ± 11	1.059
2.475	1141 ± 119	519 ± 54	1.045	2.180	611 ± 66	99.4 ± 10.7	1.055
2.574	1683 ± 175	525 ± 55	1.042	2.277	881 ± 97	91.6 ± 10.0	1.051
2.673	2309 ± 240	506 ± 53	1.040	2.379	1229 ± 137	82.6 ± 9.2	1.048
2.773	3026 ± 315	474 ± 49	1.038	2.476	1726 ± 191	78.4 ± 8.7	1.045
2.872	4018 ± 421	459 ± 48	1.036	2.577	2148 ± 237	66.5 ± 7.3	1.042
2.969	4614 ± 485	394 ± 41	1.034	2.627	3006 ± 329	77.7 ± 8.5	1.041
				2.677	2285 ± 254	49.6 ± 5.5	1.040
				2.777	1492 ± 177	23.2 ± 2.7	1.038
				2.876	1335 ± 156	15.1 ± 1.8	1.036
				3.076	698 ± 95	4.40 ± 0.60	1.032
				3.274	624 ± 96	2.32 ± 0.36	1.029
				3.473	777 ± 112	1.79 ± 0.26	1.027

where N_i^0 is the number of the nuclei of the isotope under investigation in at/cm^2 , i.e., the target number density N_i multiplied by the corresponding isotopic abundance Φ_j is the proton flux during the j th time interval Δt and n is the total number of the irradiation time intervals (bins).

In our measurements, self-absorption corrections were not necessary as the Se layers of the irradiated samples were sufficiently thin. Moreover, the HPGe detector was properly distant (15 cm) from the target surface during the off-beam activity measurements. As a result, cascade summing and pile-up effects were not significant and corrections were not necessary.

The decay properties of the Br nuclei produced in our irradiations for which (p,γ) or (p,n) reaction cross sections were measured in the present work by means of the activation technique are given in Table III, whereas the results for the screening-corrected total cross sections σ_T and the astrophysical S factors are given in Table IV. Hereby, we give only for $^{74}\text{Se}(p,\gamma)^{75}\text{Br}$ a screening correction factor f_s (second column) since it differs only in its fifth decimal place, i.e., less than 0.01%, from the respective values of the other two reactions. In the last column of Table IV, the weighted sum σ_Σ of the total cross sections of the $^{76}\text{Se}(p,\gamma)^{77}\text{Br}$ and $^{77}\text{Se}(p,n)^{77}\text{Br}$ reactions is given. The corresponding energies

TABLE III. Decay properties of the Br nuclei investigated in the present work by means of the activation technique. The third column indicates the decaying state and its spin and parity J^π in parentheses. The corresponding half-life is given in the fourth column. The last column contains the strong γ rays which, except for three superscripted with "X," were analyzed to determine the cross section of the corresponding reactions listed in the second column. Each γ ray is followed by brackets containing the corresponding relative intensity per decay I_γ (%) entering Eq. (10). The latter values were taken from [15].

Product nucleus	Producing reactions	Decaying state	Half-life	E_γ (keV)
^{75}Br	$^{74}\text{Se}(p,\gamma)$	Ground state ($3/2^-$)	96.7(13) m	141.2^X [6.6 ± 0.6], 286.5 [88 ± 5],
^{77}Br	$^{76}\text{Se}(p,\gamma)$, $^{77}\text{Se}(p,n)$	Ground state ($3/2^-$)	57.04(12) h	239.0 [23.1 ± 0.5], 520.7 [22.4 ± 0.6]
		Isomeric state ($9/2^+$)	4.28(10) m	105.9^X [13.70 ± 0.19]
^{80}Br	$^{80}\text{Se}(p,n)$	Ground state (1^+)	17.68(2) m	665.8 [1.08 ± 0.13], 616.3 [6.7 ± 0.6]
		Isomeric state (5^-)	4.4205(8) h	37.1^X [39.1 ± 0.8]
^{82}Br	$^{82}\text{Se}(p,n)$	Ground state (5^-)	35.282(7) h	554.3 [71.1 ± 0.8], 619.1 [43.5 ± 0.5], 698.4 [28.3 ± 0.4] 776.5 [83.4 ± 1.2], 827.8 [24.0 ± 0.4], 1044.0 [28.3 ± 0.4] 1317.5 [26.8 ± 0.4], 1474.9 [16.60 ± 0.23]
		Isomeric state (2^-)	6.13(5) m	619.1 [0.002 ± 0.003], 698.4 [0.034 ± 0.004] 776.5 [0.26 ± 0.03], 1317.4 [0.001 ± 0.001] 1474.9 [0.020 ± 0.003]

TABLE IV. Screening corrected total cross sections σ_T and astrophysical S factors determined in the present work at various center-of-mass energies $E_{c.m.}$ for the reactions $^{74}\text{Se}(p,\gamma)^{75}\text{Br}$ (first four columns), $^{80}\text{Se}(p,n)^{80}\text{Br}$ (next three columns), and $^{82}\text{Se}(p,n)^{82}\text{Br}$ (next three columns). A screening correction factor f_s is given (second column) only for the first reaction since its value differs only in its fifth decimal place from the respective ones of the other two reactions. In the last column, the weighted sum σ_Σ of the total cross sections of the $^{76}\text{Se}(p,\gamma)^{77}\text{Br}$ and $^{77}\text{Se}(p,n)^{77}\text{Br}$ reactions is given. The corresponding energies given in the next-to-last column are the effective energies E_{eff} in the laboratory system. The uncertainties in $E_{c.m.}$ and E_{eff} amount to 8 keV at the most.

$^{74}\text{Se}(p,\gamma)^{75}\text{Br}$				$^{80}\text{Se}(p,n)^{80}\text{Br}$			$^{82}\text{Se}(p,n)^{82}\text{Br}$			$^{76}\text{Se}(p,\gamma)$ and $^{77}\text{Se}(p,n)$	
$E_{c.m.}$	f_s	σ_T	S factor	$E_{c.m.}$	σ_T	S factor	$E_{c.m.}$	σ_T	S factor	E_{eff}	σ_Σ
(MeV)		μb	(10^4 MeV b)	(MeV)	mb	(10^4 MeV b)	(MeV)	mb	(10^4 MeV b)	(MeV)	mb
1.952	1.065	85.3 ± 9.8	446 ± 51				1.954	0.147 ± 0.014	769 ± 73	1.978	0.168 ± 0.020
2.451	1.046	463 ± 51	229 ± 25				2.455	1.21 ± 0.11	598 ± 55	2.485	0.898 ± 0.086
2.945	1.034	1203 ± 131	105 ± 11	2.948	5.06 ± 0.75	461 ± 66	2.949	5.28 ± 0.48	481 ± 44	2.985	3.15 ± 0.30
3.438	1.027	2209 ± 240	54.6 ± 5.9	3.442	18.8 ± 2.2	466 ± 53	3.443	16.1 ± 1.5	399 ± 36	3.485	9.57 ± 0.90
3.933	1.022	3804 ± 411	33.2 ± 3.6	3.937	51.5 ± 5.9	450 ± 51	3.939	41.2 ± 3.8	360 ± 33	3.987	24.6 ± 2.3
4.426	1.019	4276 ± 468	15.9 ± 1.7	4.430	71.3 ± 8.2	266 ± 30	4.431	67.1 ± 6.1	251 ± 23	4.486	32.1 ± 3.0
4.922	1.016	6585 ± 719	11.9 ± 1.3	4.927	252 ± 29	458 ± 51	4.929	147 ± 13	267 ± 24	4.989	59.3 ± 5.6
5.416	1.014	7980 ± 870	7.87 ± 0.86	5.421	398 ± 45	393 ± 44	5.423	204 ± 19	201 ± 18	5.490	86.7 ± 8.1
5.911	1.012	9042 ± 1009	5.20 ± 0.58	5.917	266 ± 30	154 ± 17	5.919	306 ± 28	178 ± 16	5.991	108 ± 10

given in the next-to-last column are the effective energies E_{eff} in the laboratory system. The relative uncertainties in the total cross sections given in Table IV do not exceed 15%. They are the result of error propagation of the statistical errors and the uncertainties in the detector efficiency (3%), the target thickness (5%), the relative intensity of the γ transitions (1–12%), and the total beam charge (7%).

IV. DISCUSSION

A. Theory of compound nucleus emission

For nuclei with an adequate number of nucleons, and a sufficiently high nucleon separation energy, capture reactions proceed through the formation of a “compound nucleus system” in an excited state. Assuming that thermal equilibrium is attained inside the compound system, the subsequent decay into any one of the open “exit” channels is treated statistically, and is completely independent of the way the compound system was formed in the “entrance” channel.

The cross section for the decay into one of the exit channels β , at center-of-mass energy E , is given by the Hauser-Feshbach (HF) compound nucleus theory [7]

$$\sigma_{\alpha\beta} = \pi \lambda_\alpha^2 \frac{1}{(2s+1)(2I+1)} \sum_{J^\pi} (2J^\pi + 1) \frac{T_\alpha^{J^\pi} T_\beta^{J^\pi}}{\sum_i T_i^{J^\pi}}, \quad (13)$$

where λ_α is the de Broglie wavelength for the “entrance” channel, I and s are the target and projectile spins, respectively, and $T_\alpha^{J^\pi}$ is the transmission coefficient summed over all orbital and channel spins to give the total transmission coefficient for the formation of the compound nucleus in state J^π . Similarly, $T_\beta^{J^\pi}$ is the total transmission coefficient for the decay of the compound nucleus into channel β , taking into account all the states of the residual system that can be populated in channel β .

The denominator in the sum of Eq. (13) contains the sum of the transmission coefficients for decay into all possible

outgoing channels i that are open at the given center-of-mass energy E . Equation (13) is furthermore multiplied by the “width fluctuation correction factor” $W_{\alpha\beta}^{J^\pi}$, to account for effects occurring when the strong elastic channel mixes with weaker absorption channels. In the cross section calculations presented in the following section, $W_{\alpha\beta}^{J^\pi}$ was taken from [21].

A compound nucleus may be excited to discrete levels as well as to states in the continuum. In the latter case, the transmission coefficients $T_\beta^{J^\pi}$ in Eq. (13) have to be replaced by averaged transmission coefficients obtained from an integral over a specified level density [22]:

$$T_\beta^{J^\pi} = \sum_{i=0}^{\omega} T_\beta^i(J^\pi) + \int_{\epsilon^\omega}^{\epsilon^{\max}} \sum_{J', \pi'} T_\beta^i(\epsilon^i, J'^{\pi'}) \rho(\epsilon^i, J'^{\pi'}) d\epsilon^i, \quad (14)$$

where the sum over the discrete levels i of the residual nucleus is taken up to the excitation energy ϵ^ω for which experimental data exist. The upper limit ϵ^{\max} of the integral on the other hand corresponds to the energy of the “entry state” of the compound nucleus, whereas $\rho(\epsilon^i, J'^{\pi'})$ is the density of nuclear states with spin $J'^{\pi'}$ at a given excitation energy ϵ^i within the integration limits.

The transmission coefficients for particle emission are determined by solving the nucleon-nucleus scattering problem with an appropriate optical model potential (OMP) [23,24] for the particle-nucleus interaction. The transmission coefficients for photon emission, however, are obtained from the γ -ray strength functions (γ SF) of the corresponding giant dipole resonance (GDR) assuming the dominance of dipole $E1/M1$ γ transitions. Different models of γ SF (empirical and microscopic) are taken from Ref. [25].

The NLDs can be obtained from microscopic calculations that take into account the discrete structure of the single-particle spectra associated with realistic effective potentials. Shell, pairing, and deformation effects are treated consistently.

NLDs from phenomenological models are calculated using primarily simple analytical formulas for which, however, drastic approximations are often made, and in which shell, pairing, and deformation effects are introduced as empirical corrections. In any case and for practical applications, both types of NLD formulas are often renormalized on existing experimental data, such as low-lying levels and s -wave neutron resonance spacings, for each nucleus.

B. Cross section calculations and comparison with experimental results

In the present work, cross section calculations were performed with the nuclear-reaction code TALYS (version 1.6) [26,27]. The code uses state-of-the-art nuclear reaction models and an updated nuclear data library [25], including the most recent experimental data and systematics, to calculate reactions in the energy range from 1 keV to 200 MeV. Information on the ground-state properties of the target and residual nuclei, such as masses, deformations, and matter densities, are obtained from experimental data or from appropriate models of the nuclear ground state as described in [26,27].

TALYS includes several OMP, NLD, and γ SF models as options. These are listed in Table V as follows: the nucleon-nucleus and α -particle-nucleus optical model potentials are denoted (first column) n OMP and α OMP, respectively. Table V contains two n OMP, five α OMP, six NLD, and five γ SF models properly abbreviated and grouped in two categories, i.e., phenomenological (second column) and semimicroscopic (third column) models. We have used all of them in all possible 300 combinations to assess the variance of the cross section values obtained from TALYS when using different n OMP, α OMP, NLD, and γ SF models. This variance in cross section values reflects the range of “uncertainties” in the cross section calculations arising from the OMPs, NLDs, and γ SFs implemented in TALYS. The model sequence n OMP- α OMP-NLD- γ SF has been adopted to refer to a specific TALYS combination, using the corresponding model abbreviations listed in Table V. In the comparison of our TALYS

calculations with experimental data, special emphasis was given to the three model combinations that we consider to be self-consistent in the sense that they combine either purely phenomenological models (TALYS-1) or semimicroscopic models (TALYS-2, TALYS-3).

TALYS-1 refers to the KD-WKD-CTFG-KU model combination of (a) n OMP of Koning and Delaroche (KD) [28], (b) TALYS-specific α OMP based on Watanabe’s folding procedure [30,31], (c) TALYS-specific constant temperature Fermi gas NLD [26], and (d) the γ SF described by the generalized Lorentzian of Kopecky and Uhl [41]. TALYS-1 is a purely phenomenological combination and is the default combination of global input parameters used by the TALYS code (version 1.6).

TALYS-2 refers to the combination JLM-B- α OMP-III-HFBCS-HFBCS/QRPA, i.e., it combines the semimicroscopic OMPs of JLM-B [29] and α OMP-III [33] with the semimicroscopic global HFBCS [38] and HFBCS/QRPA models [44] for NLDs and γ SFs, respectively. The two latter models are based on the same HFBCS model for the ground-state properties and are in this sense consistent. This combination is purely semimicroscopic.

TALYS-3 is also a combination of semimicroscopic models as it combines the OMPs of JLM-B [29] and α OMP-III [33] with the consistent HFB [39] NLDs and HFB/QRPA [25,44] γ SFs.

1. (p,γ) reactions

The experimental total cross sections σ_T determined in the present work for (p,γ) reactions are compared with the TALYS calculations in Figs. 10, 12, 13, and 14. Except for Fig. 12, they are all split into two panels: in the upper panels (a) we compare the screening-corrected total cross sections with the calculations TALYS-1 (solid curve), TALYS-2 (dashed curve), and TALYS-3 (dotted curve). The shaded areas in the panels indicate the range of “uncertainties” of the calculated cross sections arising from the models implemented in TALYS, i.e., the area covered by the different cross section calculated values resulting by using the 300 different model combinations of

TABLE V. Nuclear input parameters (first column) and corresponding phenomenological or semimicroscopic models used in our TALYS calculations. The nucleon-nucleus and alpha-particle-nucleus optical model potentials (OMP) are indicated with n OMP and α OMP, respectively. NLD and γ SF stand for nuclear level densities and γ -ray strength function, respectively.

Parameter	Phenomenological models	Semimicroscopic models
n OMP	1. KD: Global model of Koning and Delaroche [28]	2. JLM/B: Lane-consistent model of Bauge, Delaroche, and Girod [29]
α OMP	1. WKD: TALYS-specific α -particle-nucleus OMP (folding procedure of Watanabe [30,31] applied to KD [28]) 2. McFS: α -particle-nucleus OMP of McFadden and Satchler [32]	3. α OMP-I: Demetriou <i>et al.</i> (Table 1 of Ref. [33]) 4. α OMP-II: Demetriou <i>et al.</i> (Table 2 of Ref. [33]) 5. α OMP-III: Demetriou <i>et al.</i> (dispersive model in Ref. [33])
NLD	1. CTFG: Constant temperature Fermi gas [26] 2. BSFG: back-shifted Fermi gas [34,35] 3. GSM: generalized superfluid model [36,37]	4. HFBCS: Hartree-Fock-BCS [38] 5. HFB: Hartree-Fock-Bogolyubov [39] 6. HFB/T: Temperature-dependent Hartree-Fock-Bogolyubov [40]
γ SF	1. KU: Generalized Lorentzian of Kopecky and Uhl [41] 2. BA: Generalized Lorentzian of Brink and Axel [42,43]	3. HFBCS/QRPA: Hartree-Fock-BCS-quasiparticle random-phase approximation [44] 4. HFB/QRPA: Hartree-Fock-Bogolyubov-quasiparticle random-phase approximation [25,44] 5. HG: hybrid model of Goriely [45]

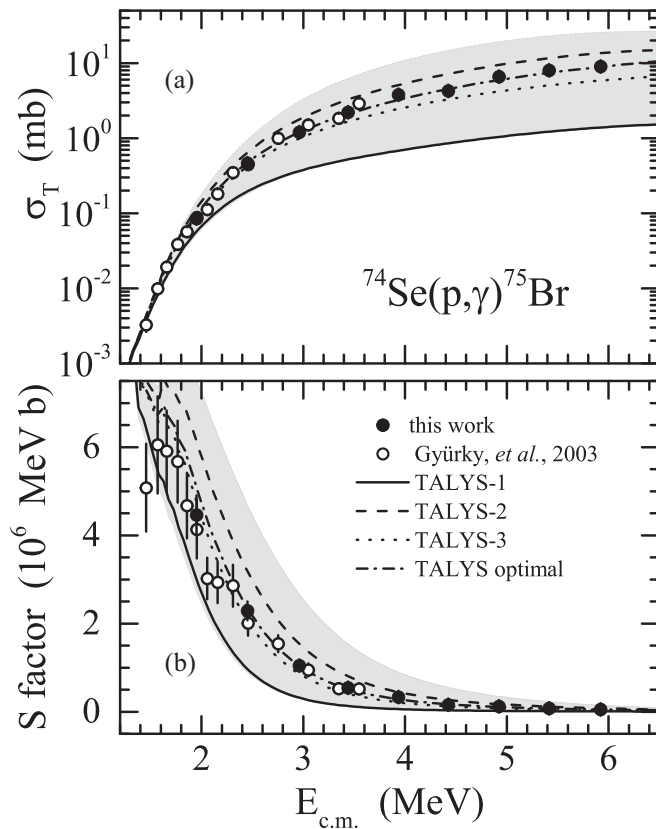


FIG. 10. Screening-corrected total cross sections (a), and corresponding S factors (b) of the $^{74}\text{Se}(p,\gamma)^{75}\text{Br}$ reaction (see Sec. IV B 1 for details).

input parameters listed in Table V. In panels (b), we show the comparison of the corresponding electron-screening corrected S factors derived from the cross sections shown in panels (a) using Eq. (8).

In Fig. 10, apart from the experimental data obtained in the present work (solid circles), we also plot the cross sections measured by Gyürky *et al.* [16], after having corrected them for electron-screening effects. As can be seen, both experimental data sets are in very good agreement. In panel (b) of the same figure, the S factors in the energy range from ≈ 2 to 3.5 MeV are reasonably reproduced by the TALYS-3 calculations (dotted curve). Below 2 MeV, the errors in the data are quite large and thus both TALYS-3 (dotted curve) and TALYS-1 (solid curve) are acceptable. At energies above 3.5 MeV, the data lie between the TALYS-3 and TALYS-2 curves (dashed curve). In addition to these three specific TALYS combinations, we plot one more labeled as “TALYS optimal” (dashed-dotted curve) which, according to a χ^2 analysis, gives the best reproduction of the experimental data. The combination that corresponds to this optimal fit is JLM/B–WKB–HFB–HFBCS/QRPA, for the n Omp, α Omp, NLD, and γ SF parameters, respectively, as listed in Table V.

For the $^{74}\text{Se}(p,\gamma)^{75}\text{Br}$ reaction, there exist additional cross section data in the literature, measured by Krivonosov *et al.* [46]. They are displayed in Fig. 11(a) after having been corrected for electron screening. As shown in this figure, they

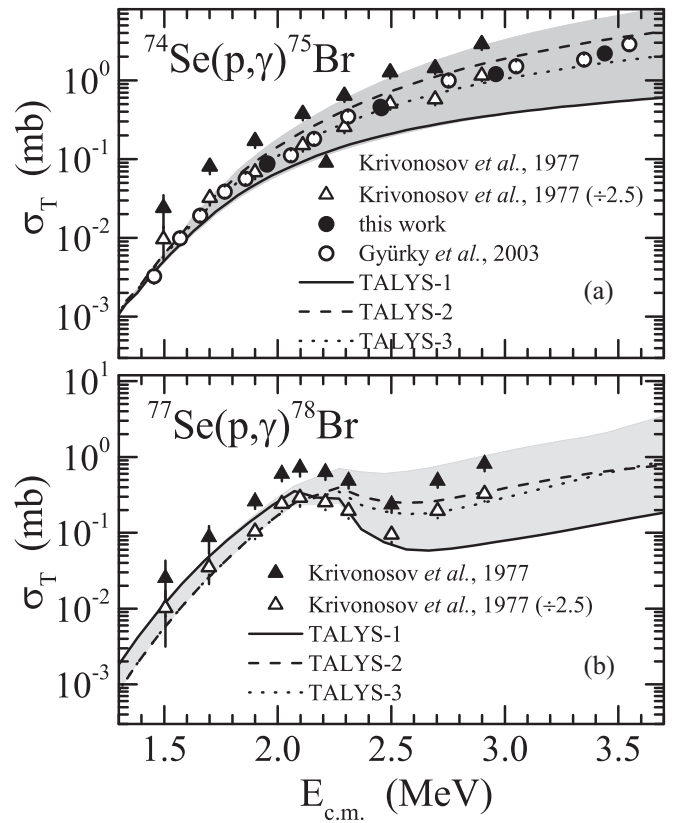


FIG. 11. Total cross sections (solid triangles) of the (a) $^{74}\text{Se}(p,\gamma)^{75}\text{Br}$ and (b) $^{77}\text{Se}(p,\gamma)^{78}\text{Br}$ reactions reported by Krivonosov *et al.* [46]. Open triangles indicate the same data divided by a factor 2.5. For comparison, in panel (a), our present results and those of Gyürky *et al.* [16] are also plotted as solid and open circles, respectively. All plotted cross sections are corrected for screening effects (see Sec. IV B 1 for details).

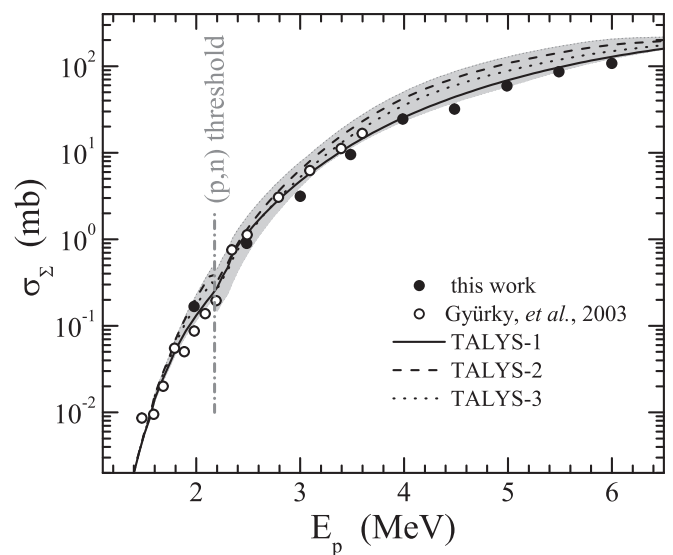


FIG. 12. Weighted sum σ_Σ of the screening-corrected total cross sections $\sigma_{(p,\gamma)}$ and $\sigma_{(p,n)}$ of $^{76}\text{Se}(p,\gamma)^{77}\text{Br}$ and $^{77}\text{Se}(p,n)^{77}\text{Br}$, respectively (see Sec. IV B 1 for details).

are by a factor of ≈ 2.5 higher than our present results and those reported in [16]. It is worth noting that the $^{77}\text{Se}(p,\gamma)^{78}\text{Br}$ reaction cross section data measured by the same authors [46] deviate from the TALYS-1, TALYS-2, and TALYS-3c calculations by a similar factor of 2.5 [see Fig. 11(b)].

As already discussed in Sec. II B, the $^{77}\text{Se}(p,n)^{77}\text{Br}$ reaction has a neutron emission threshold at 2176 keV. As a result, when natural Se targets are used in activation measurements at higher proton beam energies, the yield of the γ rays belonging to the daughter nucleus ^{77}Se (see Table III) that are present in the activation spectra is the sum of the yields due to the decaying ^{77}Br nuclei produced by the $^{77}\text{Se}(p,n)^{77}\text{Br}$ and that of the $^{76}\text{Se}(p,\gamma)^{77}\text{Br}$ reaction. Hence, the activation technique, applied in the present work with natural Se targets, allowed us to determine the cross section of the exclusive $^{76}\text{Se}(p,\gamma)^{77}\text{Br}$ reaction channel only at the lowest projectile energy measured (2 MeV). The other cross sections obtained for the $^{76}\text{Se}(p,\gamma)^{77}\text{Br}$ reaction at higher energies are in fact the sums $\sigma_{\Sigma} = \sigma_{(p,\gamma)} + \sigma_{(p,n)}$ of the $^{76}\text{Se}(p,\gamma)^{77}\text{Br}$ channel cross sections and the $^{77}\text{Se}(p,n)^{77}\text{Br}$ channel cross sections, “weighted” by their relative isotopic abundances ($^{76}\text{Se} : ^{77}\text{Se} = 1 : 0.814$). The screening-corrected σ_{Σ} data measured in the present work are compared with the TALYS calculations and the corresponding data of Gyürky *et al.* [16] in Fig. 12. The TALYS curves plotted in Fig. 12 are also weighted sums of the two contributing channels as described above. The vertical dashed-dotted line indicates the threshold (2.176 MeV)

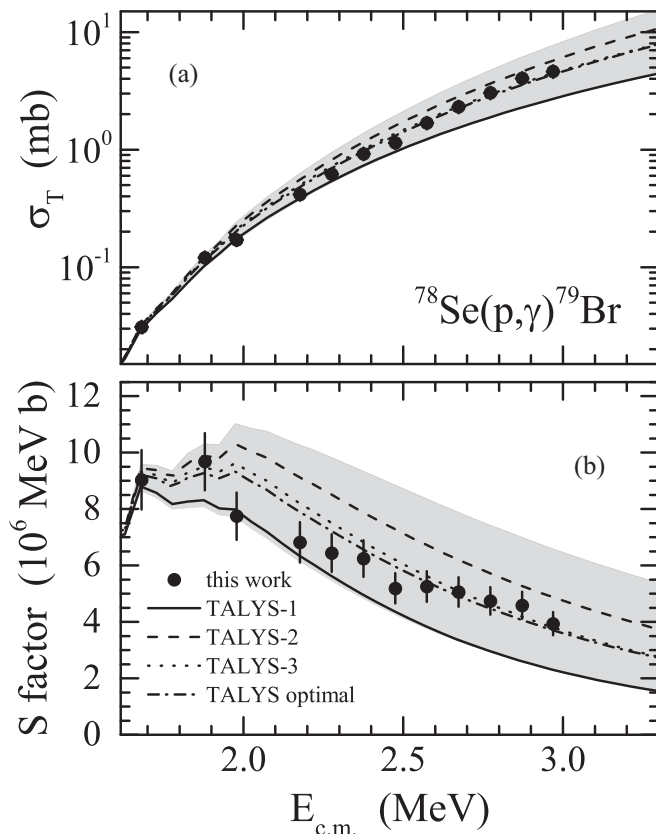


FIG. 13. Same as in Fig. 10 for the $^{78}\text{Se}(p,\gamma)^{79}\text{Br}$ reaction (see Sec. IV B 1 for details).

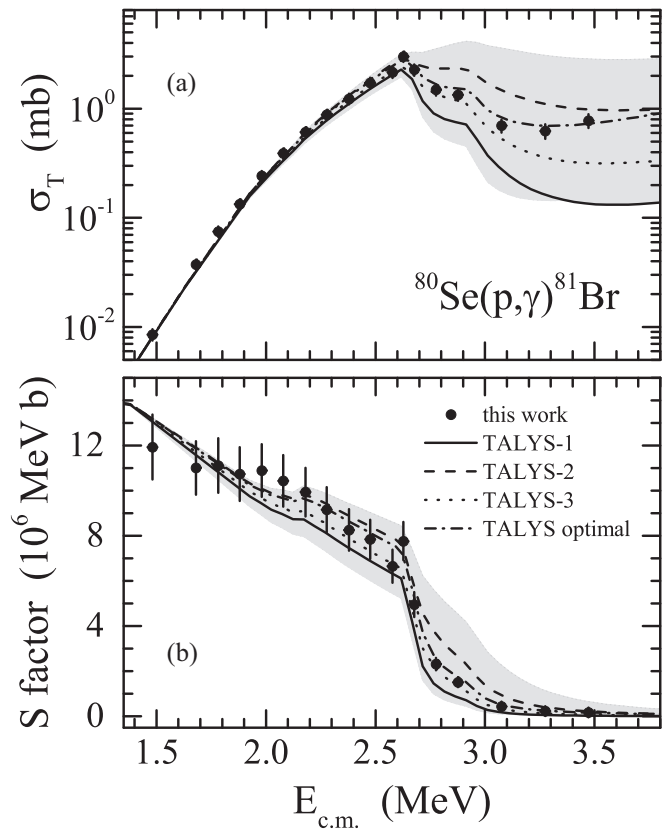


FIG. 14. Same as in Fig. 10 for the $^{80}\text{Se}(p,\gamma)^{81}\text{Br}$ reaction (see Sec. IV B 1 for details).

of the (p,n) reaction. Hence, data points below this energy are the screening-corrected $\sigma_{(p,\gamma)}$ values. The shaded areas denote the range of uncertainties associated with the calculated cross sections using the 300 different combinations of nuclear input models available in TALYS.

For the remaining two reactions $^{78}\text{Se}(p,\gamma)^{79}\text{Br}$ and $^{80}\text{Se}(p,\gamma)^{81}\text{Br}$ investigated in the present work (see Figs. 13 and 14, respectively), the findings are similar to those described above for the $^{74}\text{Se}(p,\gamma)^{75}\text{Br}$ reaction. At energies below ≈ 2.6 MeV, the experimental cross sections of the $^{78}\text{Se}(p,\gamma)^{79}\text{Br}$ reaction lie between the TALYS-1 and TALYS-3 curves. At higher energies they are clearly closer to the TALYS-3 calculations. The TALYS optimal calculations resulting from a χ^2 analysis, as discussed above, in the case of $^{78}\text{Se}(p,\gamma)^{79}\text{Br}$, correspond to the model combination JLM/B–WKD–HFBCS–KU as listed in Table V. In the case of $^{80}\text{Se}(p,\gamma)^{81}\text{Br}$, the TALYS-1, TALYS-2, and TALYS-3 curves do not differ significantly at energies below the opening of the neutron emission channel (2.686 MeV) and lie within the experimental errors. Therefore, it is not clear which model combination is best. In this case, TALYS optimal refers to the combination KD–WKD–HFB/T–BA.

2. Isomeric ratios

Apart from total cross sections for the $^{78}\text{Se}(p,\gamma)^{79}\text{Br}$ and $^{80}\text{Se}(p,\gamma)^{81}\text{Br}$ reactions, partial cross sections for the formation of ^{79}Br and ^{81}Br at excited isomeric states have also been determined in the present work. ^{79}Br has an isomeric

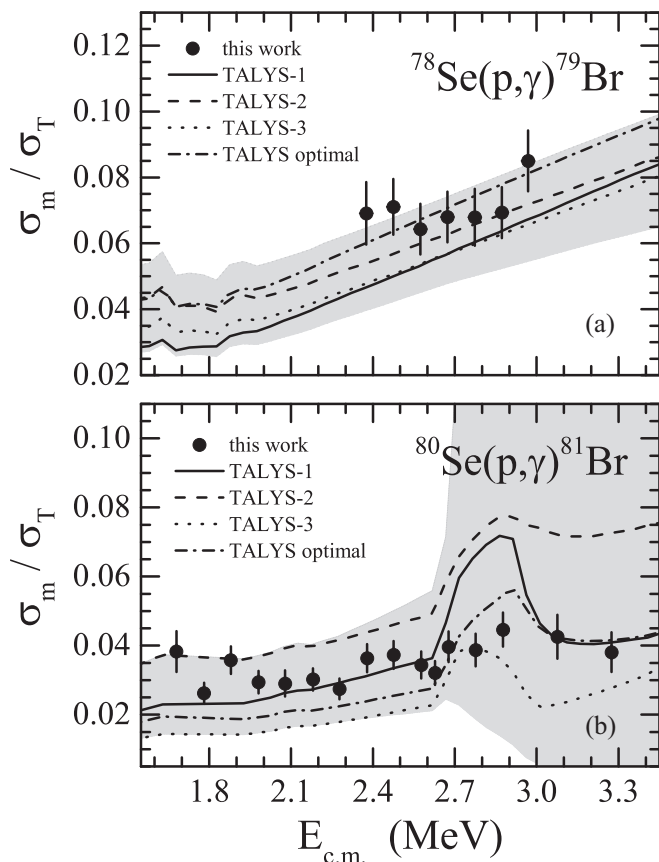


FIG. 15. Ratios σ_m/σ_T for $^{78}\text{Se}(p,\gamma)^{79}\text{Br}$ and $^{80}\text{Se}(p,\gamma)^{81}\text{Br}$, in panels (a) and (b), respectively. The TALYS “optimal” model calculations depicted in both panels with dashed-dotted curves correspond to those explained in Sec. IV B 1.

state at an excitation energy of 207.6 keV with $J^\pi = 9/2^+$ and $T_{1/2} = 4.86$ s [15]. Due to the relatively poor statistics in the corresponding γ -ray deexciting this isomer and feeding the ground state below 2.4 MeV, the relevant partial cross section could be determined only at higher energies. ^{81}Br also has an isomeric state ($J^\pi = 9/2^+$ and $T_{1/2} = 34.6$ μs) at 536.2 keV that decays to the first excited state at 276 keV [15]. The corresponding γ transition with energy 260.2 keV was strong enough to be analyzed at all beam energies. The ratios of the partial (“metastable”) cross sections over the corresponding total cross sections are plotted in Fig. 15 together with the corresponding TALYS calculations and the associated shaded areas, for both $^{78}\text{Se}(p,\gamma)^{79}\text{Br}$ and $^{80}\text{Se}(p,\gamma)^{81}\text{Br}$ reactions.

For completeness, in Fig. 16 we compare our TALYS calculations with the screening-corrected cross section data of Daly *et al.* [47] for the $^{82}\text{Se}(p,\gamma)^{83}\text{Br}$ reaction. Apart from an overall good agreement between Daly’s data and the calculations TALYS-1, -2, and 3 in the 10–12-MeV region, in the 8–10-MeV energy region the data deviate from the TALYS-1, -2, -3 curves though they are still within the shaded area, while at energies above 12 MeV the data deviate significantly from all the calculations. The deviation observed at the higher energies, above 12 MeV, is expected since with increasing energy other reaction mechanisms start competing with compound nucleus

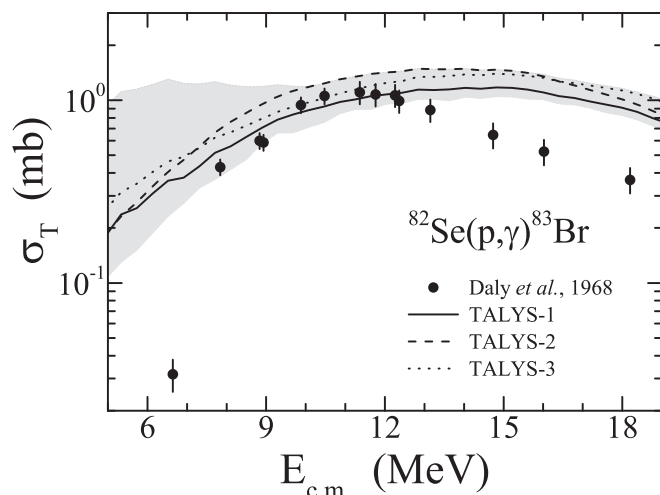


FIG. 16. Same as in Fig. 10 but for $^{82}\text{Se}(p,\gamma)^{83}\text{Br}$ [47].

reactions such as pre-equilibrium reactions. On the other hand, the discrepancy of the lowest energy (≈ 6.5 -MeV data point of Daly *et al.* [47] is difficult to explain. In any case, since the threshold of the (p,n) channel is 890 keV, the data of Daly *et al.* [47] are affected by the neutron emission channel as well, and are not suitable for testing the (p,γ) channel cross sections.

3. (p,n) reactions

A survey of the EXFOR database [48] reveals several measurements of (p,n) cross sections on Se isotopes. To date, total cross sections of (p,n) reactions on ^{77}Se and ^{78}Se have

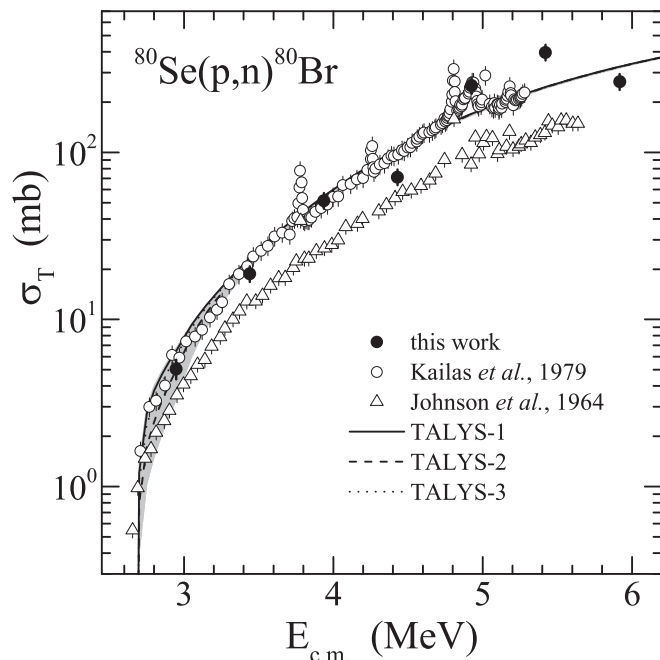


FIG. 17. Comparison of the experimental screening-corrected total cross sections σ_T from the literature [48,50,52] and the present work (solid circles) with our TALYS calculations for the $^{80}\text{Se}(p,n)^{80}\text{Br}$ reaction (see Sec. IV B 3 for details).

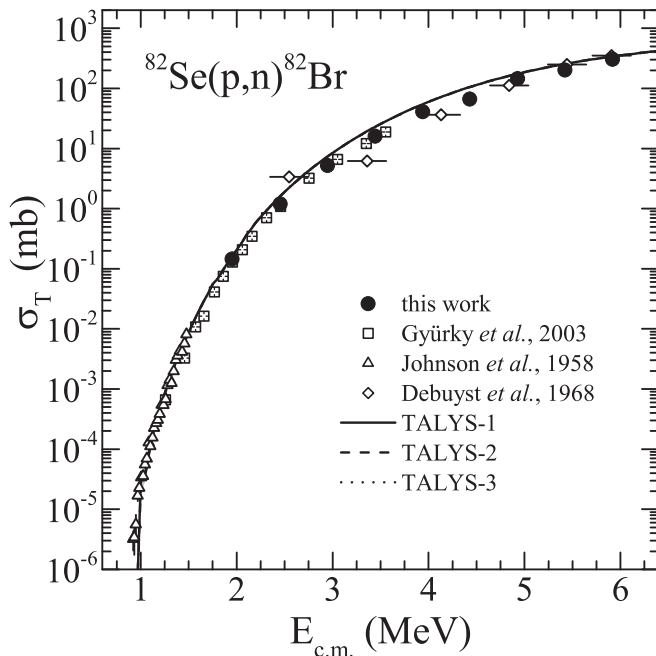


FIG. 18. Comparison of the experimental screening-corrected total cross sections σ_T existing in literature [16,49,53] and those of the present work (solid circles) with our TALYS calculations for the $^{82}\text{Se}(p,n)^{82}\text{Br}$ reaction (see also Sec. IV B 3).

been reported by Johnson *et al.* [50] and by Blaser *et al.* [51], respectively. Johnson *et al.* [48,50] and later on Kailas *et al.* [52] have published experimental total cross sections for the $^{80}\text{Se}(p,n)^{80}\text{Br}$ reaction, whereas for $^{82}\text{Se}(p,n)^{82}\text{Br}$, there exist three sets of total cross section data measured by Gyürky *et al.* [16], Debuyst *et al.* [53], and Johnson *et al.* [49].

In the present work, we have determined cross sections for the $^{80}\text{Se}(p,n)^{80}\text{Br}$ and $^{82}\text{Se}(p,n)^{82}\text{Br}$ reactions using the activation technique. The measured cross sections (listed in Table IV) are compared with the aforementioned experimental data from the literature in Figs. 17 and 18, respectively.

As shown in Fig. 17 for the $^{80}\text{Se}(p,n)^{80}\text{Br}$ reaction, our first three data points (solid circles) are in good agreement with the TALYS calculations, whereas the last four data points at higher energies are scattered around the TALYS curves. The data of Kailas *et al.* [52] (open circles) are in very good agreement with the calculations except for the “peaks” at $E_{c.m.} = 3.78, 4.26, 4.81,$ and 5.02 MeV which correspond to the isobaric analog resonances. Below ≈ 3.4 MeV the data of Kailas *et al.* [52] are well contained within the shaded area of the TALYS calculations. This shaded region almost vanishes with increasing energy where the TALYS-1, TALYS-2, and TALYS-3 results almost coincide. At these energies (above ≈ 3.4 MeV), the neutron channel is by far the dominant one and as a result the HF cross section is sensitive only to the proton OMP in the incident channel. Hence, the agreement between TALYS-1 and TALYS-2 and -3 reflects the agreement between the two proton OMPs used in these combinations, namely the OMP of JLM/B and KD. Finally, the energy dependence of the older cross sections of Johnson *et al.* [48,50] (open triangles)

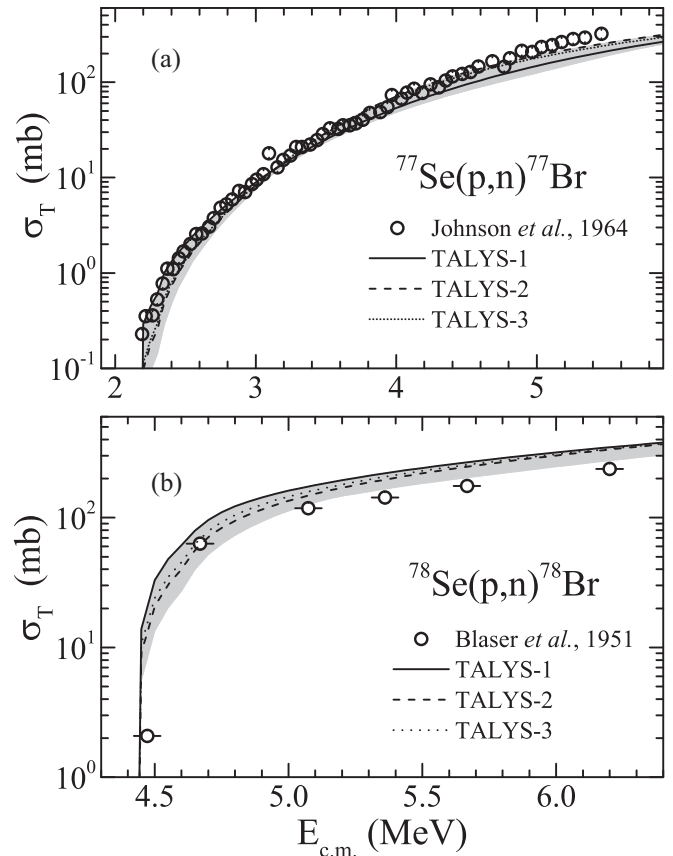


FIG. 19. Total cross sections from [50,51] for the (a) $^{77}\text{Se}(p,n)^{77}\text{Br}$ and (b) $^{78}\text{Se}(p,n)^{78}\text{Br}$ reactions compared with our TALYS calculations (see Sec. IV B 2 for details).

agrees with the TALYS calculations, however the data are by a factor ≈ 1.75 lower than the calculations.

In Fig. 18, once again the various TALYS curves do not differ significantly due to the agreement between the proton OMPs JLM/B and KD (see Table V). In fact the cross sections calculated with the different TALYS combinations for the $^{82}\text{Se}(p,n)^{82}\text{Br}$ reaction differ by $\approx 8\%$ at the most. At energies around 1 MeV, the data of Johnson *et al.* [49], which lie almost on the TALYS curves, have relative errors between 30% and 50%. At higher energies these errors range from 10 to 20%. Our data (solid circles) and those from Ref. [16] are lower than the TALYS calculations by an overall factor ≈ 1.2 and ≈ 1.5 , respectively. The experimental cross sections of Debuyst *et al.* [53] do not display the same energy dependence as the TALYS predictions, however, the uncertainties in the energies are quite large (200 keV) since the measurements were performed using a cyclotron. The differences observed between calculations and experimental data indicate that the nucleon OMPs JLM/B and KD slightly overestimate the neutron emission channel.

Cross section calculations for the $^{77}\text{Se}(p,n)^{77}\text{Br}$ and $^{78}\text{Se}(p,n)^{78}\text{Br}$ reactions are compared with the corresponding experimental data of [50] and [51], respectively, in Fig. 19. In the former case, the experimental data up to ≈ 4 MeV are in very good agreement with the calculations, whereas at higher energies they are by a factor of 1.2–1.3 higher than the

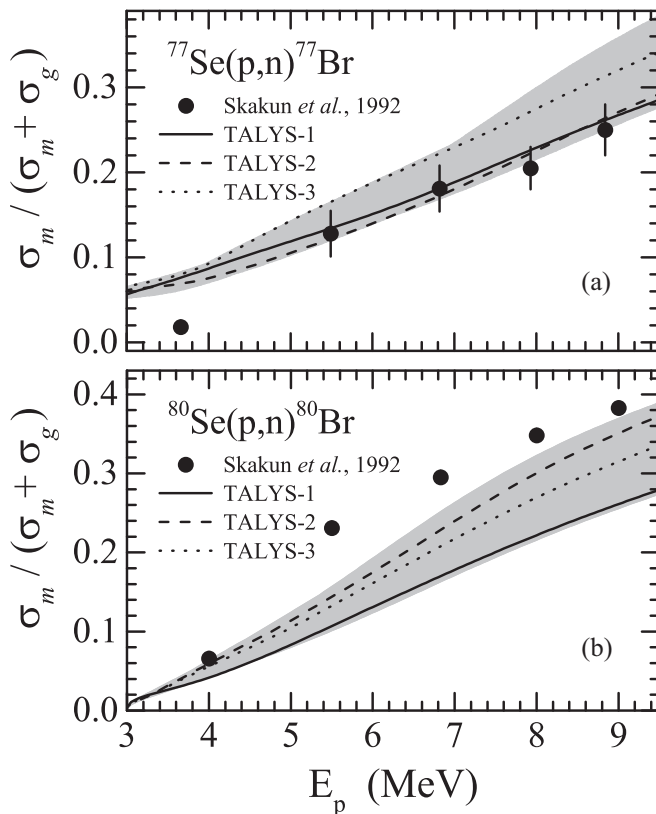


FIG. 20. Experimental ratios $\sigma_m/(\sigma_m + \sigma_g)$ from Ref. [54] compared in panel (a) and (b) with our TALYS calculations for the $^{77}\text{Se}(p,n)^{77}\text{Br}$ and $^{80}\text{Se}(p,n)^{80}\text{Br}$ reactions, respectively (see Sec. IV B 3 for details).

calculations. In the case of $^{78}\text{Se}(p,n)^{78}\text{Br}$, the data measured at energies above 4.7 MeV deviate from the calculations by 30–50%. From the shaded areas shown in panels (a) and (b), it appears that in these cases the (p,n) channel is still in competition with other open channels and hence the cross section is influenced by other nuclear parameters apart from the nucleon OMP, such as the NLDs and γ SFs.

Cross section ratios in ^{77}Br , ^{80}Br , and ^{82}Br produced via (p,n) reactions have been published by Skakun *et al.* [54,55]. Additional data for ^{80}Br have been reported by Debuyst *et al.* [53] and and Boehm *et al.* [56]. Cross section ratios between a metastable and ground state could provide an additional test of the nuclear level density (NLD) models used in Hauser-Feshbach calculations, in particular of the spin distribution.

In the case of ^{77}Br and ^{80}Br , the data shown in Fig. 20 correspond to the ratio $\sigma_m/(\sigma_m + \sigma_g)$, where σ_g refers to the cross section for the production of ^{77}Br and ^{80}Br nuclei in their ground state and σ_m for their production in corresponding $J^\pi = 9/2^+$ and 5^- metastable states at 105.86 and 85.84 keV, respectively. The corresponding half-lives are 4.28 m and 4.42 h, respectively [15]. In the case of ^{80}Br and ^{82}Br nuclei, the cross section ratios that are compared in Fig. 21 with the corresponding TALYS calculations refer to σ_g/σ_m and $\sigma_g/(\sigma_m + \sigma_g)$, respectively, with the σ_m for ^{82}Br corresponding to its $J^\pi = 2^-$ metastable state at 45.95 keV ($T_{1/2} = 6.13$ m).

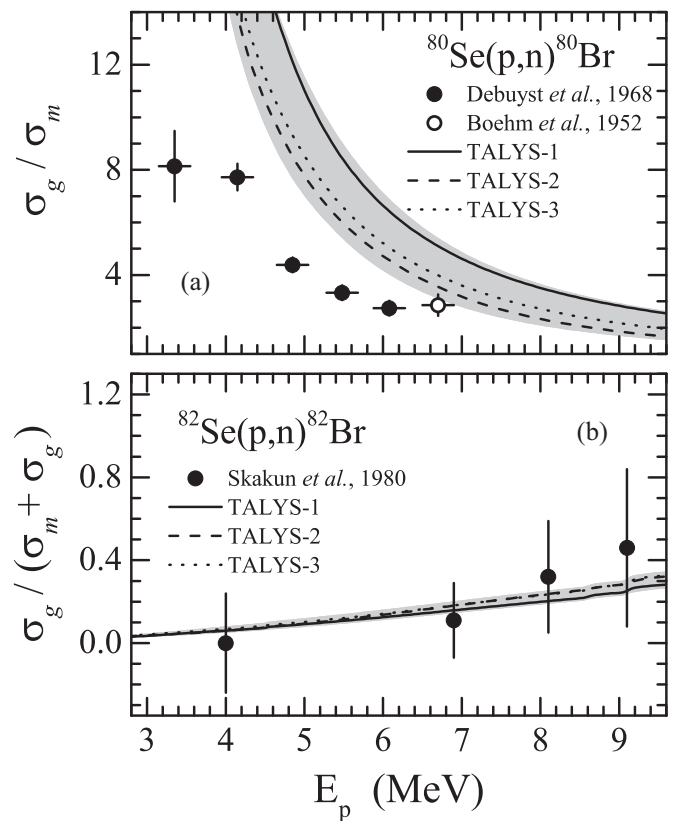


FIG. 21. Comparison of our TALYS calculations with the experimental ratios σ_g/σ_m reported in [53,56] for the $^{80}\text{Se}(p,n)^{80}\text{Br}$ reaction and $\sigma_g/(\sigma_m + \sigma_g)$ reported in [55] for $^{82}\text{Se}(p,n)^{82}\text{Br}$ (see Sec. IV B 3 for details).

As shown in Fig. 20, the cross section ratios obtained with TALYS-1 and TALYS-2 for ^{77}Br do not differ significantly and are furthermore in excellent agreement with the experimental data. This holds also for the ^{82}Br case in Fig. 21(b), for which TALYS-3 also reproduces the data. In the case of ^{80}Br , the ratios plotted in Figs. 20(b) and 21(a) lie outside the shaded area of the TALYS calculations. Of the three specific combinations TALYS-1, -2, and -3, the TALYS-2 curves deviate less from the data.

C. Reaction rates

In this section, the range of uncertainties in the cross section calculations, i.e., the range of different cross section values resulting from the TALYS calculations using different n OMP, α OMP, NLD, and γ SF models, are investigated in terms of their potential impact on the p -process nucleosynthesis calculations. These uncertainties are indicated by the shaded areas in Figs. 10, 13, and 14. p -process abundance calculations involve the solution of huge networks of nuclear reactions, including 20 000 reactions and 2000 nuclides. Due to the exceedingly large number of nuclides and reaction rates involved, we have to rely on global models of the nuclear ingredients of the HF cross section calculations (listed in Table V), which are able to provide—to the extent that it is possible—reliable predictions over a wide mass range.

The p process is assumed to occur at temperatures ranging from 1.8 to 3.3 billion K that are maintained for about 1 s. In the case of the Se isotopes, this temperature range corresponds to proton-beam energies from ≈ 1.3 to ≈ 3.9 MeV. Our present measurements cover a good part of the Gamow energy window mentioned above, so they are most relevant for (a) testing the global models entering the cross section calculations (i.e., the three global model combinations TALYS-1, TALYS-2, and TALYS-3) and their uncertainties and, most importantly, (b) for estimating how these uncertainties propagate into the reaction rates, which are actually used in abundance calculations.

The ground-state reaction rates $RR = N_A \langle \sigma v \rangle$, often referred to as laboratory reaction rates, were derived from the total cross sections σ_T obtained using the TALYS code, for different temperatures T by

$$N_A \langle \sigma v \rangle = \sqrt{\frac{8}{\pi \mu}} \frac{N_A}{(kT)^{3/2}} \int_0^\infty \sigma_T(E) E e^{-E/kT} dE, \quad (15)$$

where N_A is the Avogadro number, μ is the reduced mass, kT is the thermal energy, and E is the center-of-mass energy. TALYS also provides stellar reaction rates that are calculated using partition functions based on experimental excited spectra, whenever available [25], or on the basis of the nuclear level densities obtained from the HFB plus combinatorial method [39]. In the following, stellar rates are labeled as rr to be distinguished from the ground-state reaction rates RR .

From the systematic comparison of TALYS-1, TALYS-2, and TALYS-3 calculations with experimental cross sections presented in Sec. IV B, we have found that TALYS-3 performs fairly well, as it reproduces the experimental cross section data satisfactorily and at the same time is global and ensures consistency between the Hartree-Fock-Bogolyubov models used to calculate the masses, the NLDs, and γ SFs. We therefore use this combination to elaborate its impact on the reaction rates. In Fig. 22 we compare the ratios RR_0/RR_3 for the

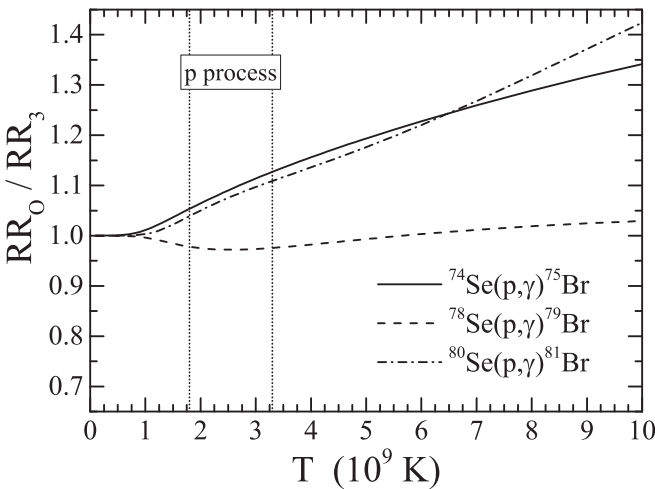


FIG. 22. Ratios of the ground-state reaction rates RR_0 over RR_3 for $^{74}\text{Se}(p,\gamma)^{75}\text{Br}$ (solid curve), $^{78}\text{Se}(p,\gamma)^{79}\text{Br}$ (dashed curve), and $^{80}\text{Se}(p,\gamma)^{81}\text{Br}$ (dashed-dotted curve). RR_0 have been derived from the TALYS “optimal” combinations. RR_3 are the reaction rates deduced from the TALYS-3 calculations.

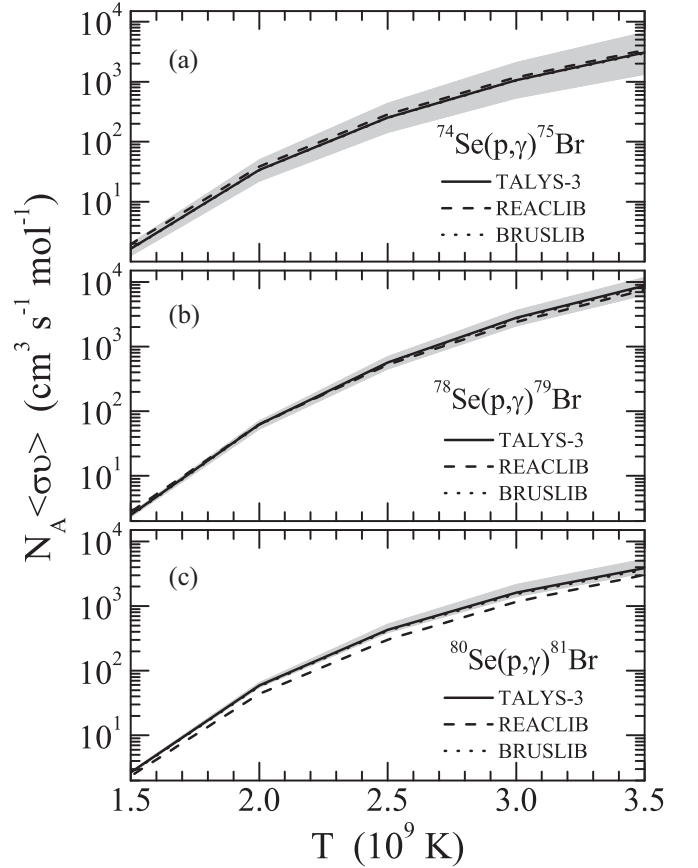


FIG. 23. Stellar reaction rates of the $^{74}\text{Se}(p,\gamma)^{75}\text{Br}$, $^{78}\text{Se}(p,\gamma)^{79}\text{Br}$, and $^{80}\text{Se}(p,\gamma)^{81}\text{Br}$ reactions at temperatures relevant to p process. The shaded areas and TALYS-3 calculations (solid curves) are explained in the caption of Fig. 10 and in Sec. IV B. The corresponding REACLIB [57] and BRUSLIB [58] rates are indicated by the dashed and dotted curves, respectively.

three (p,γ) reactions studied herein, where RR_3 refers to the ground-state reaction rates obtained using the TALYS-3 combination, and RR_0 refers to those obtained by using the TALYS combination labeled “TALYS optimal.” The latter, according to a χ^2 analysis, gives the best reproduction of the experimental data shown in Figs. 10, 13, 14, and 15.

From Fig. 22 one can see that, within the p -process relevant temperature region indicated by the vertical dotted lines, the “TALYS optimal” combination deviates from TALYS-3 by a factor of 1.10, i.e., by 10% at most. Such a deviation is considerably smaller than the factor of 3 that is considered to be acceptable for deviations between calculated p -nuclei abundances and the observed solar-system abundances.

Using Eq. (15), we calculated the corresponding stellar reaction rates $rr = N_A \langle \sigma v \rangle_i$ at temperatures relevant to the p process for all 300 TALYS model combinations i (see Sec. IV A), for all three (p,γ) reactions investigated in the present work. The results are shown in Fig. 23, whereby the corresponding TALYS-3 stellar rates are indicated by solid curves, whereas the remaining 299 sets of different stellar reaction rates form a band of uncertainties that is indicated by shaded areas. There is a one-to-one correspondence between the shaded areas in

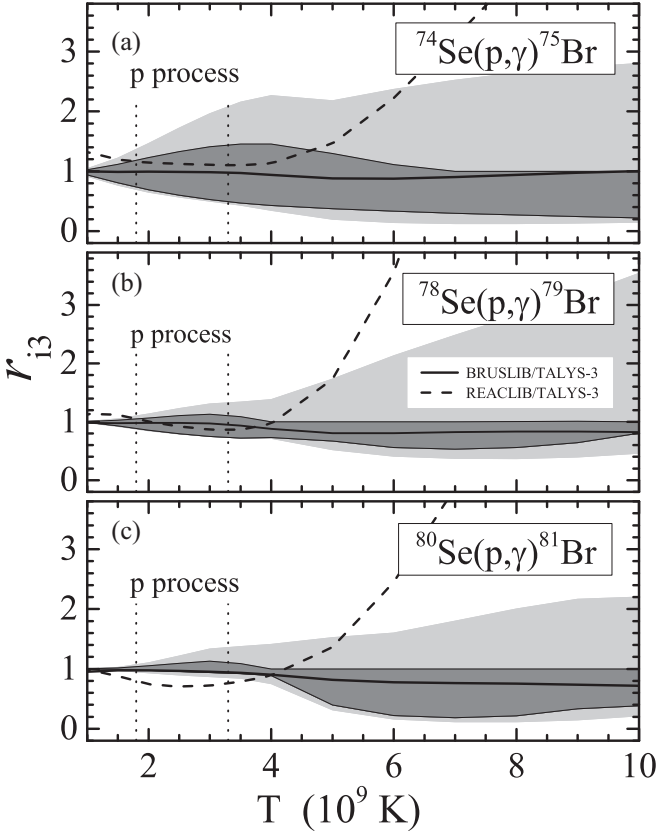


FIG. 24. Ratios r_{i3} of the upper and lower calculated stellar reaction rates over the global TALYS-3 combination of the n OMP, α OMP, NLD, and γ SF models (see text for details). The solid and dashed curves indicate the stellar reaction-rate ratios of those given in the BRUSLIB [58] and REACLIB [57] databases, respectively, over the corresponding ones calculated using the global TALYS-3 combination.

this figure and those in Figs. 10, 13, and 14. In Fig. 23, we plot also (dotted curve) the stellar rates extracted from the REACLIB database [57] as well as those available in the BRUSLIB [58] database. From Fig. 23 it is clear that, in the case of $^{74}\text{Se}(p,\gamma)^{75}\text{Br}$ the differences between the three sets of stellar reaction rates are very small. In fact, the BRUSLIB rates almost coincide with those obtained with the TALYS-3 combination. On the other hand, the REACLIB values tend to decrease with respect to TALYS-3 and BRUSLIB as we go from panel (a) to panel (c), where they are clearly the lowest.

In Fig. 24, we plot the ratios $r_{i3} = \langle \sigma v \rangle_i / \langle \sigma v \rangle_3$, where $\langle \sigma v \rangle_i$ are the upper and lower limits of all the calculated stellar reaction rates for each of the (p,γ) reactions, and $\langle \sigma v \rangle_3$ are the corresponding stellar reaction rates obtained from the TALYS-3 combination.

From this figure one can clearly see that, for all three nuclides studied herein, the uncertainties in the stellar rates (shaded areas) due to the uncertainties in the HF calculations are considerably reduced (dark-grey shaded areas) when the reaction rate calculations are constrained within the maximum and minimum values provided by the combinations

TALYS-1 and TALYS-2 (dark-grey shaded areas). More specifically, the maximum reaction-rate uncertainties in the case of $^{74}\text{Se}(p,\gamma)^{75}\text{Br}$, $^{78}\text{Se}(p,\gamma)^{79}\text{Br}$, and $^{80}\text{Se}(p,\gamma)^{81}\text{Br}$ are reduced by 50%, 25%, and 30%, respectively. It is worth noting that, within the p -process temperature limits, the minimum and maximum values of the dark-shaded area vary from ≈ 0.5 to 1.5 for the ^{74}Se case, ≈ 0.7 to 1.2 for ^{78}Se , and ≈ 0.9 to 1.1 for ^{80}Se . The range of uncertainties due to nuclear models is thus well within the average discrepancies observed between calculated p -nuclei abundances and observations that range between 0.3 and 3.

In Fig. 24, we also plot the ratio of the stellar rates from the REACLIB database [57] over the stellar rates obtained using the TALYS-3 combination. Similarly, the dotted curve is the ratio of the stellar rates from the BRUSLIB [58] database over the TALYS-3 reaction rates. The same trend observed in Fig. 23 for the REACLIB values is observed also in Fig. 24. The REACLIB rates decrease with increasing mass number of the isotope. In the case of ^{80}Se , the ratio of the REACLIB stellar rates over the TALYS-3 rates has a minimum value of 0.70 within the temperature range relevant to p process that is indicated by the vertical dotted lines, while in panels (a) and (b), it ranges from ≈ 0.9 to 1.1. Within the same p -process temperature limits, the ratio of the BRUSLIB stellar rates to the TALYS-3 rates are ≈ 1 for all three reactions.

For use in astrophysics applications, the ground-state rates calculated in the present work with the TALYS-3 model combination for the $^{74}\text{Se}(p,\gamma)^{75}\text{Br}$, $^{78}\text{Se}(p,\gamma)^{79}\text{Br}$, and $^{80}\text{Se}(p,\gamma)^{81}\text{Br}$ reactions are given in Table VI, together with upper and lower limits, which correspond to the region of uncertainties of the TALYS calculations also shown in Figs. 10, 13, and 14.

V. CONCLUSIONS

In the present work the total cross sections of proton capture reactions on ^{74}Se , ^{78}Se , and ^{80}Se isotopes were determined at energies relevant to p -process nucleosynthesis. In the case of ^{74}Se , the activation technique was applied at beam energies from 2 to 6 MeV, whereas in the case of ^{78}Se and ^{80}Se isotopes, cross sections were determined by measuring in-beam γ -angular distributions at incident proton energies between 1.5 and 3.5 MeV. The cross section data as well as the resulting astrophysical S factors were compared with Hauser-Feshbach calculations obtained with the nuclear reaction code TALYS [26] using combinations of global semimicroscopic and phenomenological models of optical potentials (OMPs), nuclear level densities (NLDs), and γ -ray strength functions (γ SFs).

Although the calculated cross sections and related S factors show a non-negligible scatter due to the uncertainties affecting the OMP, NLD, and γ SF, it was found that the TALYS-3 combination of the semimicroscopic OMP of Bauge *et al.* [29] with the microscopic HFB NLDs of Hilaire and Goriely [39] and HFB/QRPA γ SFs reported in [25,44] gives an overall good description of the data.

Isomeric cross section ratios were also determined for the $^{78}\text{Se}(p,\gamma)^{79}\text{Br}$ and $^{80}\text{Se}(p,\gamma)^{81}\text{Br}$ reactions, and were compared with TALYS results. Overall, reasonable agreement

TABLE VI. Laboratory reaction rates RR obtained in the present work using Eq. (15). The RR values of the second, fifth, and eighth columns are the reaction rates (in $\text{cm}^3 \text{s}^{-1} \text{mol}^{-1}$) derived for the $^{74}\text{Se}(p,\gamma)^{75}\text{Br}$, $^{78}\text{Se}(p,\gamma)^{79}\text{Br}$, and $^{80}\text{Se}(p,\gamma)^{81}\text{Br}$ reactions, respectively, using the model combination TALYS-3. The corresponding lower (RR_{low}) and upper (RR_{high}) limits correspond to the lower and upper limits of the shaded areas of Figs. 10, 13, and 14, respectively (see also text).

T_9	$^{74}\text{Se}(p,\gamma)^{75}\text{Br}$			$^{78}\text{Se}(p,\gamma)^{79}\text{Br}$			$^{80}\text{Se}(p,\gamma)^{81}\text{Br}$		
	RR	RR_{low}	RR_{high}	RR	RR_{low}	RR_{high}	RR	RR_{low}	RR_{high}
0.1	5.79×10^{-48}	5.76×10^{-48}	5.80×10^{-48}	8.99×10^{-48}	8.99×10^{-48}	8.99×10^{-48}	1.78×10^{-47}	1.78×10^{-47}	1.78×10^{-47}
0.15	1.29×10^{-31}	1.28×10^{-31}	1.29×10^{-31}	2.05×10^{-31}	2.05×10^{-31}	2.05×10^{-31}	3.96×10^{-31}	3.96×10^{-31}	3.96×10^{-31}
0.2	1.92×10^{-23}	1.91×10^{-23}	1.92×10^{-23}	3.09×10^{-23}	3.09×10^{-23}	3.09×10^{-23}	5.61×10^{-23}	5.61×10^{-23}	5.61×10^{-23}
0.25	1.62×10^{-18}	1.61×10^{-18}	1.62×10^{-18}	2.62×10^{-18}	2.62×10^{-18}	2.62×10^{-18}	4.40×10^{-18}	4.40×10^{-18}	4.40×10^{-18}
0.3	3.33×10^{-15}	3.30×10^{-15}	3.34×10^{-15}	5.34×10^{-15}	5.34×10^{-15}	5.34×10^{-15}	8.31×10^{-15}	8.31×10^{-15}	8.31×10^{-15}
0.4	5.38×10^{-11}	5.31×10^{-11}	5.40×10^{-11}	8.41×10^{-11}	8.40×10^{-11}	8.41×10^{-11}	1.15×10^{-10}	1.15×10^{-10}	1.15×10^{-10}
0.5	2.10×10^{-8}	2.06×10^{-8}	2.11×10^{-8}	3.20×10^{-8}	3.19×10^{-8}	3.20×10^{-8}	4.01×10^{-8}	4.01×10^{-8}	4.01×10^{-8}
0.6	1.26×10^{-6}	1.22×10^{-6}	1.27×10^{-6}	1.87×10^{-6}	1.87×10^{-6}	1.88×10^{-6}	2.23×10^{-6}	2.23×10^{-6}	2.23×10^{-6}
0.7	2.56×10^{-5}	2.43×10^{-5}	2.61×10^{-5}	3.74×10^{-5}	3.72×10^{-5}	3.75×10^{-5}	4.34×10^{-5}	4.34×10^{-5}	4.35×10^{-5}
0.8	2.64×10^{-4}	2.46×10^{-4}	2.73×10^{-4}	3.81×10^{-4}	3.77×10^{-4}	3.82×10^{-4}	4.37×10^{-4}	4.35×10^{-4}	4.37×10^{-4}
0.9	1.73×10^{-3}	1.57×10^{-3}	1.82×10^{-3}	2.48×10^{-3}	2.44×10^{-3}	2.49×10^{-3}	2.82×10^{-3}	2.81×10^{-3}	2.83×10^{-3}
1	8.26×10^{-3}	7.24×10^{-3}	8.90×10^{-3}	1.18×10^{-2}	1.15×10^{-2}	1.19×10^{-2}	1.33×10^{-2}	1.32×10^{-2}	1.34×10^{-2}
1.1	3.11×10^{-2}	2.63×10^{-2}	3.46×10^{-2}	4.46×10^{-2}	4.29×10^{-2}	4.56×10^{-2}	5.03×10^{-2}	4.96×10^{-2}	5.08×10^{-2}
1.2	9.77×10^{-2}	7.98×10^{-2}	1.13×10^{-1}	1.42×10^{-1}	1.35×10^{-1}	1.47×10^{-1}	1.60×10^{-1}	1.56×10^{-1}	1.62×10^{-1}
1.3	2.67×10^{-1}	2.10×10^{-1}	3.19×10^{-1}	3.98×10^{-1}	3.70×10^{-1}	4.19×10^{-1}	4.43×10^{-1}	4.31×10^{-1}	4.54×10^{-1}
1.4	6.49×10^{-1}	4.93×10^{-1}	8.07×10^{-1}	1.00	9.11×10^{-1}	1.07	1.10	1.06	1.14
1.5	1.44	1.05	1.86	2.29	2.05	2.50	2.51	2.40	2.63
1.6	2.93	2.08	3.95	4.88	4.27	5.44	5.30	5.00	5.62
1.7	5.60	3.85	7.85	9.71	8.32	1.11×10^1	1.04×10^1	9.75	1.12×10^1
1.8	1.01×10^1	6.73	1.47×10^1	1.83×10^1	1.53×10^1	2.12×10^1	1.94×10^1	1.79×10^1	2.12×10^1
1.9	1.73×10^1	1.12×10^1	2.61×10^1	3.26×10^1	2.69×10^1	3.88×10^1	3.42×10^1	3.13×10^1	3.81×10^1
2	2.84×10^1	1.79×10^1	4.44×10^1	5.58×10^1	4.52×10^1	6.77×10^1	5.77×10^1	5.23×10^1	6.54×10^1
2.1	4.49×10^1	2.75×10^1	7.25×10^1	9.18×10^1	7.30×10^1	1.14×10^2	9.33×10^1	8.36×10^1	1.08×10^2
2.2	6.85×10^1	4.10×10^1	1.14×10^2	1.46×10^2	1.14×10^2	1.84×10^2	1.45×10^2	1.29×10^2	1.71×10^2
2.3	1.01×10^2	5.93×10^1	1.75×10^2	2.24×10^2	1.73×10^2	2.89×10^2	2.19×10^2	1.93×10^2	2.62×10^2
2.4	1.46×10^2	8.37×10^1	2.59×10^2	3.35×10^2	2.55×10^2	4.42×10^2	3.19×10^2	2.79×10^2	3.90×10^2
2.5	2.06×10^2	1.15×10^2	3.75×10^2	4.89×10^2	3.66×10^2	6.56×10^2	4.54×10^2	3.93×10^2	5.65×10^2
2.6	2.84×10^2	1.56×10^2	5.32×10^2	6.97×10^2	5.15×10^2	9.53×10^2	6.30×10^2	5.41×10^2	7.98×10^2
2.7	3.83×10^2	2.06×10^2	7.37×10^2	9.73×10^2	7.09×10^2	1.36×10^3	8.54×10^2	7.28×10^2	1.10×10^3
2.8	5.08×10^2	2.69×10^2	1.00×10^3	1.33×10^3	9.59×10^2	1.89×10^3	1.13×10^3	9.60×10^2	1.49×10^3
2.9	6.63×10^2	3.44×10^2	1.34×10^3	1.79×10^3	1.28×10^3	2.59×10^3	1.48×10^3	1.24×10^3	1.98×10^3
3	8.53×10^2	4.36×10^2	1.77×10^3	2.38×10^3	1.67×10^3	3.49×10^3	1.90×10^3	1.58×10^3	2.59×10^3
3.1	1.08×10^3	5.44×10^2	2.30×10^3	3.10×10^3	2.16×10^3	4.63×10^3	2.40×10^3	1.99×10^3	3.32×10^3
3.2	1.36×10^3	6.71×10^2	2.94×10^3	3.99×10^3	2.75×10^3	6.06×10^3	2.98×10^3	2.46×10^3	4.21×10^3
3.3	1.68×10^3	8.19×10^2	3.72×10^3	5.08×10^3	3.46×10^3	7.84×10^3	3.66×10^3	3.00×10^3	5.25×10^3
3.4	2.06×10^3	9.90×10^2	4.66×10^3	6.39×10^3	4.31×10^3	1.00×10^4	4.45×10^3	3.62×10^3	6.49×10^3
3.5	2.51×10^3	1.19×10^3	5.77×10^3	7.95×10^3	5.32×10^3	1.26×10^4	5.34×10^3	4.32×10^3	7.91×10^3
3.6	3.02×10^3	1.41×10^3	7.08×10^3	9.79×10^3	6.49×10^3	1.58×10^4	6.34×10^3	5.11×10^3	9.56×10^3
3.7	3.60×10^3	1.66×10^3	8.61×10^3	1.20×10^4	7.85×10^3	1.95×10^4	7.47×10^3	5.98×10^3	1.14×10^4
3.8	4.27×10^3	1.94×10^3	1.04×10^4	1.45×10^4	9.42×10^3	2.40×10^4	8.72×10^3	6.95×10^3	1.35×10^4
3.9	5.02×10^3	2.26×10^3	1.24×10^4	1.73×10^4	1.12×10^4	2.91×10^4	1.01×10^4	8.00×10^3	1.59×10^4
4	5.87×10^3	2.60×10^3	1.47×10^4	2.07×10^4	1.32×10^4	3.51×10^4	1.16×10^4	9.15×10^3	1.86×10^4
4.1	6.81×10^3	2.99×10^3	1.74×10^4	2.44×10^4	1.55×10^4	4.21×10^4	1.32×10^4	1.04×10^4	2.15×10^4
4.2	7.86×10^3	3.41×10^3	2.04×10^4	2.87×10^4	1.81×10^4	5.00×10^4	1.50×10^4	1.17×10^4	2.47×10^4
4.3	9.02×10^3	3.87×10^3	2.37×10^4	3.34×10^4	2.10×10^4	5.90×10^4	1.69×10^4	1.32×10^4	2.82×10^4
4.4	1.03×10^4	4.37×10^3	2.75×10^4	3.88×10^4	2.42×10^4	6.92×10^4	1.89×10^4	1.47×10^4	3.21×10^4

TABLE VI. (Continued.)

T_9	$^{74}\text{Se}(p,\gamma)^{75}\text{Br}$			$^{78}\text{Se}(p,\gamma)^{79}\text{Br}$			$^{80}\text{Se}(p,\gamma)^{81}\text{Br}$		
	RR	RR _{low}	RR _{high}	RR	RR _{low}	RR _{high}	RR	RR _{low}	RR _{high}
4.5	1.17×10^4	4.92×10^3	3.17×10^4	4.47×10^4	2.77×10^4	8.07×10^4	2.11×10^4	1.63×10^4	3.62×10^4
4.6	1.32×10^4	5.50×10^3	3.63×10^4	5.13×10^4	3.15×10^4	9.35×10^4	2.34×10^4	1.80×10^4	4.07×10^4
4.7	1.49×10^4	6.14×10^3	4.14×10^4	5.85×10^4	3.58×10^4	1.08×10^5	2.58×10^4	1.98×10^4	4.56×10^4
4.8	1.67×10^4	6.82×10^3	4.71×10^4	6.64×10^4	4.04×10^4	1.24×10^5	2.84×10^4	2.16×10^4	5.07×10^4
4.9	1.87×10^4	7.55×10^3	5.32×10^4	7.50×10^4	4.53×10^4	1.41×10^5	3.10×10^4	2.36×10^4	5.62×10^4
5	2.08×10^4	8.32×10^3	5.99×10^4	8.44×10^4	5.07×10^4	1.60×10^5	3.38×10^4	2.56×10^4	6.20×10^4
5.5	3.39×10^4	1.30×10^4	1.03×10^5	1.43×10^5	8.41×10^4	2.85×10^5	4.96×10^4	3.69×10^4	9.64×10^4
6	5.16×10^4	1.90×10^4	1.64×10^5	2.24×10^5	1.29×10^5	4.64×10^5	6.78×10^4	4.97×10^4	1.39×10^5
7	1.03×10^5	3.56×10^4	3.49×10^5	4.56×10^5	2.53×10^5	1.01×10^6	1.10×10^5	7.81×10^4	2.48×10^5
8	1.77×10^5	5.81×10^4	6.33×10^5	7.77×10^5	4.19×10^5	1.82×10^6	1.56×10^5	1.08×10^5	3.81×10^5
9	2.77×10^5	8.66×10^4	1.02×10^6	1.17×10^6	6.16×10^5	2.87×10^6	2.04×10^5	1.38×10^5	5.32×10^5
10	4.00×10^5	1.21×10^5	1.51×10^6	1.61×10^6	8.34×10^5	4.13×10^6	2.51×10^5	1.66×10^5	6.94×10^5

was found between data and model calculations implying that the spin-dependent terms of the NLDs are reliable. For completeness, we have also compared isomeric cross section ratios from the literature for the (p,n) channels of ^{77}Se , ^{80}Se , and ^{82}Se . The three main combinations of TALYS global input parameter models were able to describe the data of ^{77}Se and ^{82}Se , whereas in the case of ^{80}Se , all three combinations deviate from the data by an average factor ≈ 2 .

Total cross sections for the $^{82}\text{Se}(p,n)^{82}\text{Br}$ and $^{80}\text{Se}(p,n)^{80}\text{Br}$ reactions have also been determined in the present work by means of the activation technique. Our results were compared with other data found in the literature and with the corresponding TALYS calculations. For completeness, we also included data from the literature for the $^{78}\text{Se}(p,n)^{78}\text{Br}$ and $^{77}\text{Se}(p,n)^{77}\text{Br}$ reactions in our studies. We found that in the first three cases, the TALYS cross sections are by up to a factor ≈ 1.5 higher than the experimental data. In the case of $^{77}\text{Se}(p,n)^{77}\text{Br}$, the calculations give an overall good description of the data. It is worth mentioning, however that, in the (p,n) cases mentioned above, the TALYS calculations differ by less than 10% on average. As the existing data have comparable or even larger uncertainties, they cannot be used

to draw any conclusion on the input parameters listed in Table V.

The impact of the different TALYS combinations of nuclear input parameters (OMP, NLD, γ SF) on the ground-state reaction rates was also studied and the nuclear uncertainties propagated from the HF calculations were shown to be less than a factor of 2 which is well below the average discrepancies observed between calculated p -nuclei abundances and observations.

Our results highlight the need for a continued effort on the systematic study of proton-capture reactions in this energy and mass region to reduce the range of uncertainties arising from global nuclear models. In this regard, new independent data related to optical model potentials, nuclear level densities, and γ strength functions are of paramount importance to help constrain the corresponding global nuclear models.

ACKNOWLEDGMENT

The authors thank R. Julin from the University of Jyväskylä, Finland, for providing the enriched target material.

- [1] F. Käppeler, R. Gallino, S. Bisterzo, and W. Aoki, The s process: Nuclear physics, stellar models, and observations, *Rev. Mod. Phys.* **83**, 157 (2011).
- [2] M. Arnould, S. Goriely, and K. Takahashi, The r -process of stellar nucleosynthesis: Astrophysics and nuclear physics achievements and mysteries, *Phys. Rep.* **450**, 97 (2007).
- [3] M. Arnould and S. Goriely, The p -process of stellar nucleosynthesis: astrophysics and nuclear physics status, *Phys. Rep.* **384**, 1 (2003).
- [4] A. Sauerwein, J. Endres, L. Netterdon, A. Zilges, V. Foteinou, G. Provas, T. Konstantinopoulos, M. Axiotis, S. F. Ashley, S. Harissopulos, and T. Rauscher, Investigation of the reaction $^{74}\text{Ge}(p,\gamma)^{75}\text{As}$ using the in-beam method to improve reaction network predictions for p nuclei, *Phys. Rev. C* **86**, 035802 (2012).
- [5] A. Spyrou, S. J. Quinn, A. Simon, T. Rauscher, A. Battaglia, A. Best, B. Bucher, M. Couder, P. A. DeYoung, A. C. Dombos, X. Fang, J. Görres, A. Kontos, Q. Li, L. Y. Lin, A. Long, S. Lyons, B. S. Meyer, A. Roberts, D. Robertson *et al.*, Measurement of the $^{90,92}\text{Zr}(p,\gamma)^{91,93}\text{Nb}$ reactions for the nucleosynthesis of elements near $A = 90$, *Phys. Rev. C* **88**, 045802 (2013).
- [6] J. Mayer, S. Goriely, L. Netterdon, S. Péru, P. Scholz, R. Schwengner, and A. Zilges, Partial cross sections of the $^{92}\text{Mo}(p,\gamma)$ reaction and the γ strength in ^{93}Tc , *Phys. Rev. C* **93**, 045809 (2016).
- [7] W. Hauser and H. Feshbach, The inelastic scattering of neutrons, *Phys. Rev.* **87**, 366 (1952).
- [8] Y. Wang and S. Nastasi, *Handbook of Modern Ion Beam Materials Analysis*, 2nd ed. (Cambridge University Press, Cambridge, England, 2010).

- [9] S. Galanopoulos, P. Demetriou, M. Kokkoris, S. Harissopulos, R. Kunz, M. Fey, J. W. Hammer, G. Gyürky, Z. Fülop, E. Somorjai, and S. Goriely, The $^{88}\text{Sr}(p,\gamma)^{89}\text{Y}$ reaction at astrophysically relevant energies, *Phys. Rev. C* **67**, 015801 (2003).
- [10] S. Harissopulos, A. Spyrou, A. Lagoyannis, M. Axiotis, P. Demetriou, J. W. Hammer, R. Kunz, and H.-W. Becker, Cross section measurements of proton capture reactions relevant to the p process: The case of $^{89}\text{Y}(p,\gamma)^{90}\text{Zr}$ and $^{121,123}\text{Sb}(p,\gamma)^{122,124}\text{Te}$, *Phys. Rev. C* **87**, 025806 (2013).
- [11] K. Debertin and R. Helmer, *Gamma and X-ray Spectrometry with Semiconductor Detectors*, (North Holland, Elsevier Science, Amsterdam, 1988).
- [12] M. Kolbe, B. Beckhoff, M. Krumrey, and G. Ulm, Thickness determination for Cu and Ni nanolayers: Comparison of completely reference-free fundamental parameter-based X-ray fluorescence analysis and X-ray reflectometry, *Spectrochim. Acta, Part B* **60**, 505 (2005).
- [13] A. Markowicz and R. V. Grieken, *Handbook on X-Ray Spectrometry* (Marcel Dekker, New York, 1993).
- [14] J. F. Ziegler and J. P. Biersack, Code SRIM Version (2003). Full description given by J. F. Ziegler, J. P. Biersack, and U. Littmark, *The Stopping and Range of Ions in Solids* (Pergamon, New York, 1985).
- [15] IAEA Live Chart of Nuclides, Nuclear Structure and Decay Data based on the Evaluated Nuclear Structure Data File (ENSDF), <https://www-nds.iaea.org/livechart/>.
- [16] G. Gyürky, Z. Fulop, E. Somorjai, M. Kokkoris, S. Galanopoulos, P. Demetriou, S. Harissopulos, T. Rauscher, and S. Goriely, Proton induced reaction cross section measurements on se isotopes for the astrophysical p process, *Phys. Rev. C* **68**, 055803 (2003).
- [17] M. Mayer, SIMNRA, a simulation program for the analysis of NRA, RBS and ERDA, in *Proceedings of the 15th International Conference on the Application of Accelerators in Research and Industry*, AIP Conf. Proc. No. 475, edited by J. L. Duggan and I. L. Morgan (AIP, Melville, NY, 1999), p. 541.
- [18] C. E. Rolfs and W. S. Rodney, *Cauldrons in the Cosmos* (The University of Chicago Press, Chicago, 1988).
- [19] C. E. Rolfs, Enhanced electron screening in metals: A plasma for the poor man, *Nucl. Phys. News* **16**, 9 (2006); (private communication).
- [20] K. U. Kettner, H. W. Becker, F. Strieder, and C. Rolfs, High-Z electron screening: The cases $^{50}\text{V}(p,n)^{50}\text{Cr}$ and $^{176}\text{Lu}(p,n)^{176}\text{Hf}$, *J. Phys. G: Nucl. Part. Phys.* **32**, 489 (2006).
- [21] P. A. Moldauer, Statistics on the average cross section, *Nucl. Phys. A* **344**, 185 (1980).
- [22] G. R. Satchler, *Introduction to Nuclear Reactions* (Oxford University Press, New York, 1990).
- [23] P. E. Hodgson, E. Gadioli, and E. Gadioli Erba, *Introductory Nuclear Physics* (Oxford University Press, New York, 1997).
- [24] C. A. Bertulani and P. Danielewicz, *Introduction to Nuclear Reactions* (IOP Publishing Ltd, Bristol, 2004).
- [25] R. Capote, M. Herman, P. Obložinský, P. G. Young, S. Goriely, T. Belgia, A. V. Ignatyuk, A. J. Koning, S. Hilaire, V. Plujko, M. Avrigeanu, O. Bersillon, M. B. Chadwick, T. Fukahori, S. Kailas, J. Kopecky, V. M. Maslov, G. Reffo, M. Sin, E. Soukhovitskii *et al.*, RIPL - Reference input parameter library for calculation of nuclear reactions and nuclear data evaluations, *Nucl. Data Sheets* **110**, 3107 (2009).
- [26] A. J. Koning, S. Hilaire, and M. C. Duijvestijn, TALYS-1.0, in *Proceedings of the International Conference on Nuclear Data for Science and Technology, Nice, France, 2007*, edited by O. Bersillon, F. Gunsing, E. Bauge, R. Jacqmin, and S. Leray (EDP Sciences, Les Ulis, France, 2008), p. 211 (available online at <http://dx.doi.org/10.1051/ndata:07767>).
- [27] Nuclear-reaction code TALYS-1.6 (available online at <http://www.talys.eu/home>).
- [28] A. J. Koning and J. P. Delaroche, Local and global nucleon optical models from 1 keV to 200 MeV, *Nucl. Phys. A* **713**, 231 (2003).
- [29] E. Bauge, J. P. Delaroche, and M. Girod, Lane-consistent, semimicroscopic nucleon-nucleus optical model, *Phys. Rev. C* **63**, 024607 (2001).
- [30] S. Watanabe, High energy scattering of deuterons by complex nuclei, *Nucl. Phys.* **8**, 484 (1958).
- [31] D. G. Madland, Recent results in the development of a global medium-energy nucleon-nucleus optical-model potential, in *Proceedings of a Specialists' Meeting on Preequilibrium Nuclear Reactions, Semmering, Austria, 1988*, edited by B. Strohmaier (OECD, Paris, 1988), p. 103.
- [32] L. McFadden and G. R. Satchler, Optical-model analysis of the scattering of 24.7 MeV alpha particles, *Nucl. Phys.* **84**, 177 (1966).
- [33] P. Demetriou, C. Grama, and S. Goriely, Improved global α -optical model potentials at low energies, *Nucl. Phys. A* **707**, 253 (2002).
- [34] W. Dilg, W. Schantl, H. Vonach, and M. Uhl, Level density parameters for the back-shifted fermi gas model in the mass range $40 < A < 250$, *Nucl. Phys. A* **217**, 269 (1973).
- [35] M. K. Grossjean and H. Feldmeier, Level density of a Fermi gas with pairing interactions, *Nucl. Phys. A* **444**, 113 (1985).
- [36] A. V. Ignatyuk, K. K. Istekov, and G. N. Smirenkin, The role of collective effects in the systematics of nuclear level densities, *Yad. Fiz.* **29**, 875 (1979) [*Sov. J. Nucl. Phys.* **29**, 450 (1979)].
- [37] A. V. Ignatyuk, J. L. Weil, S. Raman, and S. Kahane, Density of discrete levels in ^{116}Sn , *Phys. Rev. C* **47**, 1504 (1993).
- [38] P. Demetriou and S. Goriely, Microscopic nuclear level densities for practical applications, *Nucl. Phys. A* **695**, 95 (2001).
- [39] S. Goriely, S. Hilaire, and A. J. Koning, Improved microscopic nuclear level densities within the Hartree-Fock-Bogoliubov plus combinatorial method, *Phys. Rev. C* **78**, 064307 (2008).
- [40] S. Hilaire, M. Girod, S. Goriely, and A. J. Koning, Temperature-dependent combinatorial level densities with the DIM Gogny force, *Phys. Rev. C* **86**, 064317 (2012).
- [41] J. Kopecky and M. Uhl, Test of gamma-ray strength functions in nuclear reaction model calculations, *Phys. Rev. C* **41**, 1941 (1990).
- [42] D. M. Brink, Individual particle and collective aspects of the nuclear photoeffect, *Nucl. Phys.* **4**, 215 (1957).
- [43] P. Axel, Electric dipole ground-state transition width strength function and 7-mev photon interactions, *Phys. Rev.* **126**, 671 (1962).
- [44] E. Khan, S. Goriely, D. Allard, E. Parizot, T. Suomijarvi, A. J. Koning, S. Hilaire, and M. C. Duijvestijn, Photodisintegration of ultra-high-energy cosmic rays revisited, *Astropart. Phys.* **23**, 191 (2005).
- [45] S. Goriely, Radiative neutron captures by neutron-rich nuclei and the r -process nucleosynthesis, *Phys. Lett. B* **436**, 10 (1998).

- [46] G. A. Krivonosov, O. L. Ekchichev, B. A. Nemashkalo, V. E. Storizhko, and V. K. Chirt, Radiative capture cross-section of protons by medium atomic weight nuclei at low energy, *Izv. Akad. Nauk SSSR, Ser. Fiz.* **41**, 2196 (1977) [*Bull. Acad. Sci. USSR, Phys. Ser.* **41**, 175 (1977)]; Experimental Nuclear Reaction Data (EXFOR), <https://www-nds.iaea.org/exfor/exfor.htm>.
- [47] P. J. Daly, B. M. Seppelt, and P. F. D. Shaw, Radiative capture cross sections in medium-weight and heavy nuclei, *Nucl. Phys. A* **119**, 673 (1968).
- [48] N. Otuka, E. Dupont, V. Semkova, B. Pritychenko, A. I. Blokhin, M. Aikawa, S. Babykina, M. Bossant, G. Chen, S. Dunaeva, R. A. Forrest, T. Fukahori, N. Furutachi, S. Ganesan, Z. Ge, O. O. Gritzay, M. Herman, S. Hlavač, K. Katō, B. Lalremruata, Y. O. Lee, A. Makinaga, K. Matsumoto, M. Mikhaylyukova, G. Pikulina, V. G. Pronyaev, A. Saxena, O. Schwerer, S. P. Simakov, N. Soppera, R. Suzuki, S. Takács, X. Tao, S. Taova, F. Tárkányi, V. V. Varlamov, J. Wang, S. C. Yang, V. Zerkin, and Y. Zhuang, Towards a more complete and accurate experimental nuclear reaction data library (EXFOR): International collaboration between nuclear reaction data centres (NRDC), *Nucl. Data Sheets* **120**, 272 (2014); Experimental Nuclear Reaction Data (EXFOR), <https://www-nds.iaea.org/exfor/exfor.htm>.
- [49] C. H. Johnson, A. Galonsky, and J. P. Ulrich, Proton strength functions from (p, n) cross sections, *Phys. Rev.* **109**, 1243 (1958).
- [50] C. H. Johnson, C. C. Trail, and A. Galonsky, Thresholds for (p, n) reactions on 26 intermediate-weight nuclei, *Phys. Rev.* **136**, B1719 (1964); Experimental Nuclear Reaction Data (EXFOR), <https://www-nds.iaea.org/exfor/exfor.htm>.
- [51] J. P. Blaser, F. Boehm, P. Marmier, and P. Scherrer, Anregungsfunktionen und Wirkungsquerschnitte der (p,n)-Reaktion (II), *Helv. Phys. Acta* **24**, 441 (1951); Experimental Nuclear Reaction Data (EXFOR), <https://www-nds.iaea.org/exfor/exfor.htm>.
- [52] S. Kailas, S. Saini, M. K. Mehta, N. Veerabahu, Y. P. Viyogi, and N. K. Ganguly, Isobaric analog resonances in the $^{80}\text{Se}(p, n)^{80}\text{Br}$ reaction, *Nucl. Phys. A* **315**, 157 (1979).
- [53] R. Debuyst and A. Vander Stricht, Excitation functions and yield ratios for the isomeric pair Br-80/Br-80m formed in (d, 2n), (α , np), (α , p) and (p, n) reactions on selenium, *J. Inorg. Nucl. Chem.* **30**, 691 (1968).
- [54] E. A. Skakun and V. G. Batij, Level density parameters from excitation cross sections of isomeric states, *Z. Phys. A* **344**, 13 (1992).
- [55] E. A. Skakun, V. G. Batij, Ju. N. Rakivnenko, V. A. Lucik, and I. A. Romanij, Cross section ratios for producing isomeric pairs of $^{77m.g}\text{Br}$, $^{80m.g}\text{Br}$ and $^{82m.g}\text{Br}$ in (p, n) reactions, in *Proceeding of the Conference on Nuclear Spectroscopy and Nuclear Structure, Leningrad, 1980* (AN SSSR, Moscow, 1980), p. 324; Experimental Nuclear Reaction Data (EXFOR), <https://www-nds.iaea.org/exfor/exfor.htm>.
- [56] F. Boehm, P. Marmier, and P. Preiswerk, Relative Wirkungsquerschnitte für die Anregung von Isomeren und Grundzuständen durch die (pn)-Reaktion, *Helv. Phys. Acta* **25**, 599 (1952); Experimental Nuclear Reaction Data (EXFOR), <https://www-nds.iaea.org/exfor/exfor.htm>.
- [57] R. H. Cyburt, A. M. Amthor, R. Ferguson, Z. Meisel, K. Smith, S. Warren, A. Heger, R. D. Hoffman, T. Rauscher, A. Sakharuk, H. Schatz, F. K. Thielemann, and M. Wiescher, The Jina reaclib database: Its recent updates and impact on type-IX-ray bursts, *Astrophys. J. Suppl. Ser.* **189**, 240 (2010).
- [58] Y. Xu, S. Goriely, A. Jorissen, G. L. Chen, and M. Arnould, Databases and tools for nuclear astrophysics applications: BRUSsels Nuclear LIBrary (BRUSLIB), Nuclear Astrophysics Compilation of REactions II (NACRE II) and Nuclear NETwork GENerator (NETGEN), *Astron. Astrophys.* **549**, A106 (2013).